LMC Calls, Milky Way Halo Answers: Disentangling the Effects of the MW–LMC Interaction on Stellar Stream Populations

Richard A. N. Brooks[1,2] , Nicolás Garavito-Camargo[2] , Kathryn V. Johnston[3] , Adrian M. Price-Whelan[2] ,
Jason L. Sanders[1] , and Sophia Lilleengen[4]
[1] Department of Physics and Astronomy, University College London, London, WC1E 6BT, UK; richard.brooks.22@ucl.ac.uk
[2] Center for Computational Astrophysics, Flatiron Institute, Simons Foundation, 162 Fifth Avenue, New York, NY 10010, USA
[3] Department of Astronomy, Columbia University, New York, NY 10027, USA
[4] Institute for Computational Cosmology, Department of Physics, Durham University, South Road, Durham DH1 3LE, UK

Abstract

The infall of the LMC into the Milky Way (MW) has dynamical implications throughout the MW's dark matter halo. We study the impact of this merger on the statistical properties of populations of simulated stellar streams. Specifically, we investigate the radial and on-sky angular dependence of stream perturbations caused by the direct effect of stream–LMC interactions and/or the response of the MW dark matter halo. We use a time-evolving MW–LMC simulation described by basis function expansions to simulate streams. We quantify the degree of perturbation using a set of stream property statistics including the misalignment of proper motions with the stream track. In the outer halo, direct stream–LMC interactions produce a statistically significant effect, boosting the fraction of misaligned proper motions by ∼25% relative to the model with no LMC. Moreover, there is on-sky angular dependence of stream perturbations: the highest fractions of perturbed streams coincide with the same on-sky quadrant as the present-day LMC location. In the inner halo, the MW halo dipole response primarily drives stream perturbations, but it remains uncertain whether this is a detectable signature distinct from the LMC's influence. For the fiducial MW–LMC model, we find agreement between the predicted fraction of streams with significantly misaligned proper motions, $\bar{\vartheta} > 10°$, and Dark Energy Survey data. Finally, we predict this fraction for the Rubin Observatory Legacy Survey of Space and Time (LSST) footprint. Using LSST data will improve our constraints on dark matter models and LMC properties, as it is sensitive to both.

1. Introduction

Our Galaxy, the Milky Way (MW) is undergoing a merger with the LMC.[5] The LMC is thought to be on its first pericentric passage and to have a dark matter mass $M_{LMC} \sim 10^{11} M_{\odot}$ (G. Besla et al. 2007, 2010; M. Boylan-Kolchin et al. 2011; J. Peñarrubia et al. 2016; A. Kravtsov & S. Winney 2024). An alternative scenario has the LMC on its second pericentric passage (E. Vasiliev 2024); although, most features of the earlier passage are superseded by the more recent passage at a smaller pericenter. Many Local Group phenomena require a large mass for the LMC to explain, for example: the kinematics of MW satellites (L. Correa Magnus & E. Vasiliev 2022; A. Kravtsov & S. Winney 2024), dynamical models of stellar streams (D. Erkal et al. 2019a; S. E. Koposov et al. 2019; N. Shipp et al. 2021; E. Vasiliev et al. 2021), and the timing argument (J. Peñarrubia et al. 2016, but see also D. Benisty et al. 2022; K. Chamberlain et al. 2023; D. Benisty 2024). The LMC has also been observed to generate significant disequilibrium in the MW gravitational potential: the displacement of the MW disk (M. S. Petersen & J. Peñarrubia 2020; E. Vasiliev et al. 2021), a stellar overdensity (V. Belokurov et al. 2019;

N. Garavito-Camargo et al. 2019; C. Conroy et al. 2021; J. A. S. Amarante et al. 2024), and the reflex motion of the stellar halo (D. Erkal et al. 2019a, 2021; M. S. Petersen & J. Peñarrubia 2020, 2021; V. Chandra et al. 2024; R. Yaaqib et al. 2024). The orbit of the LMC is sensitive to the assumed Galactic potential (see Figure 3 of E. Vasiliev 2023) and, because the LMC is of considerable mass, it is also subject to dynamical friction from the MW dark matter halo (S. Chandrasekhar 1943). Current state-of-the-art models of the MW–LMC system account for dynamical friction and the reflex motion of both galaxies (e.g., F. A. Gómez et al. 2015; E. Patel et al. 2017, 2020; D. Erkal et al. 2019b; N. Garavito-Camargo et al. 2019, 2021; E. C. Cunningham et al. 2020; E. Vasiliev et al. 2021; A. M. Dillamore et al. 2022; K. Donaldson et al. 2022; S. E. Koposov et al. 2023; S. Lilleengen et al. 2023; E. Vasiliev 2024).

Stellar streams form when satellites, dwarf galaxies, or globular clusters orbiting the MW tidally disrupt. Stellar streams are kinematic tracers of the Galactic potential (A. Helmi & S. D. M. White 1999; K. V. Johnston et al. 1999) as stars within a stream roughly delineate orbits in the host potential (T. A. McGlynn 1990; K. V. Johnston et al. 1996; J. Binney 2008; J. L. Sanders & J. Binney 2013). This allows us to infer the accelerations that the stars' experience and hence the host's gravitational field. In the MW, we know of ∼170 globular clusters (E. Vasiliev & H. Baumgardt 2021) and ∼80 MW stellar streams[6] associated with globular clusters or

---

[5] The Large Milky/Magellanic Cloud. See E. Vasiliev (2023) for a comprehensive review detailing the effect of the LMC on the MW.

---

[6] See A. Bonaca & A. M. Price-Whelan (2025) for a review of MW streams in the Gaia era (Gaia Collaboration et al. 2021).

coming from fully disrupted globular clusters (C. Mateu 2023). Most of the detected globular cluster streams are within a Galactocentric distance of $\lesssim 35$ kpc. However, the current number of known MW streams (C. Mateu 2023) is likely not the full population in the MW (N. Shipp et al. 2023; S. Pearson et al. 2024), and we can expect to discover many more with future surveys, e.g., the Rubin Observatory Legacy Survey of Space and Time (LSST; Ž. Ivezić et al. 2019), out to much greater Galactocentric distances of ~ 75 kpc.

At a Galactocentric distance of ~ 50 kpc (G. Pietrzyński et al. 2019), the LMC has perturbed streams in the MW, especially those with close encounters (e.g., Orphan-Chenab, D. Erkal et al. 2019a; N. Shipp et al. 2021; S. E. Koposov et al. 2023; S. Lilleengen et al. 2023; R. A. N. Brooks et al. 2024). As we expect to uncover more outer halo MW streams (S. Pearson et al. 2024), it is useful to predict the extent to which the LMC has left them dynamically perturbed. Testing these predictions will allow us to learn the properties of the LMC itself. Additionally, the Galactic suburbs are ideal for studying deformations of streams caused by interactions with dark matter subhaloes from both the MW and LMC (e.g., J. H. Yoon et al. 2011; J. L. Sanders et al. 2016; D. Erkal et al. 2017; A. Bonaca et al. 2019, 2020; K. Tavangar et al. 2022; A. Bonaca & A. M. Price-Whelan 2025; T. Hilmi et al. 2024) because of fewer additional disturbances from dynamical resonances and baryonic interactions in the inner parts of our Galaxy (e.g., A. M. Price-Whelan et al. 2016; S. Pearson et al. 2017; D. Kawata et al. 2021). In fact, the frequency of subhalo–stream interactions and the resulting perturbed stream properties are dependent on the underlying cosmological model (e.g., cold versus warm dark matter; R. G. Carlberg et al. 2024a, 2024b). Therefore, it is of great importance for us to further disentangle perturbations due to small-scale structure, i.e., dark matter subhaloes, and/or bulk effects such as the LMC.

As the LMC (a satellite galaxy), falls into the gravitational potential of the MW (the central galaxy), the host responds by generating a density wake (S. Chandrasekhar 1943). This is because an infalling satellite will have a broad range of orbital frequencies that resonate with dark matter particles of the host galaxy (W. A. Mulder 1983; M. D. Weinberg 1986). The classical "conic" wake trailing the LMC is described as the *transient response*, whereas the response elsewhere in the MW halo is the *collective response* caused by the amplitude of the barycenter displacement (N. Garavito-Camargo et al. 2019, 2021; T. Tamfal et al. 2021; H. R. Foote et al. 2023). The detailed structure of these deformations depends on the nature of dark matter itself (e.g., S. R. Furlanetto & A. Loeb 2002; L. Hui et al. 2017; L. Lancaster et al. 2020). The density wake of the LMC is predicted to leave an observable signature in the density and kinematics of MW halo stars (e.g., C. Conroy et al. 2021; M. Cavieres et al. 2024), including those in stellar streams. Any perturbations due to the wake will be most striking in the outer halo trailing the past orbit of the LMC, $\gtrsim 50$ kpc (e.g., E. Vasiliev 2023). However, there are very few streams that have been detected at, or beyond, these distances to date.

Basis function expansions (BFEs) are used to represent general mass distributions as linear combinations of basis functions. As such, BFEs offer the flexibility to model the deformations captured in N-body simulations (E. J. Lilley et al. 2018a, 2018b; M. S. Petersen & J. Peñarrubia 2020;

J. L. Sanders et al. 2020; N. Garavito-Camargo et al. 2021; S. Lilleengen et al. 2023). In this work, we use the N-body simulation of S. Lilleengen et al. (2023), which utilizes a BFE description using the EXP toolkit (M. S. Petersen et al. 2022). This provides a time-evolving MW system in which stellar streams can be generated. These simulations account for the deformations to the MW and LMC dark matter haloes since the latter's infall, including the formation of a dark matter dynamical friction wake trailing the LMC. Studies of N-body MW–LMC simulations act as complementary efforts to MW–LMC analogs identified from cosmological simulations (e.g., the *Milky Way-est* cold dark matter, and DREAMS warm dark matter, zoomed-in simulations; D. Buch et al. 2024; J. C. Rose et al. 2024, respectively).

Perturbations to streams caused by interactions with the LMC have been studied for a handful of known MW streams, e.g., the LMC has been attributed to the misalignment of proper motions in the Orphan-Chenab stream (D. Erkal et al. 2019b), the Sagittarius stream (E. Vasiliev et al. 2021), and for the Dark Energy Survey (DES; N. Shipp et al. 2018, 2019) streams, with the stream perturbations being a sensitive tracer of the properties of the LMC (e.g., its mass; D. Erkal et al. 2019b; N. Shipp et al. 2021; S. E. Koposov et al. 2023). In this work, we will statistically determine the extent of two distinct effects on simulated populations of realistic MW stellar streams. Specifically, we will investigate the radial and on-sky angular dependence of stream perturbations caused by: direct interactions with the LMC and/or the MW halo deforming in response to the infalling LMC. We will compare predictions to the current observational data from DES and make predictions for what LSST can expect to observe. These predictions are sensitive to: (i) the underlying dark matter model, e.g., varying the dark matter model on galaxy cluster scales alters the galaxy-dark matter offset, density profile, and subhalo distribution (S. Y. Kim et al. 2017; A. Banerjee et al. 2020). As gravity is scale-invariant, similar behavior is expected in the MW (e.g., O. Sameie et al. 2018). And (ii) the properties of the LMC, e.g., a more/less massive LMC would increase/decrease the fraction of streams displaying significant perturbations. Hence, future observations in conjunction with flexible models of the MW–LMC will allow us to better constrain the nature of dark matter and properties of the LMC.

The plan of the paper is as follows. Section 2 describes our methodology including an overview of BFEs, the Galactic potentials used in this study, and the framework to generate stellar streams. In Section 3, we present the distribution of stream statistics for the population of MW streams made in each potential. Further, we demonstrate the detectable signatures of the LMC and MW halo response seen in the stream properties. In Section 4, we compare our results for proper-motion misalignments with observational data. In Section 5 we discuss our results in context and assess any caveats. Finally, we summarize and conclude our results in Section 6.

2. Methods

To generate stellar stream models in a time-evolving MW–LMC system, we need to describe the potential, density, and forces at any arbitrary position and time. Rigid, non-time-evolving potentials fail to capture deformations to the MW and LMC dark matter haloes. We use BFEs, described in Section 2.1.1, to expand and evolve the N-body models of

the MW and LMC as outlined in Section 2.1.2. Using the BFE description for the Galactic potential, we generate populations of globular cluster streams in Section 2.2.

2.1. Generating a Flexible Potential Model

2.1.1. Basis Function Expansions

BFEs offer a framework to describe these time-dependent deformations. They track the gravitational potential, density, and forces as the system evolves over time. BFEs have previously been seen to accurately describe flexible models of the MW (M. S. Petersen et al. 2016, 2019; B. Dai et al. 2018; M. S. Petersen & J. Peñarrubia 2020; N. Garavito-Camargo et al. 2021). In this work, we use the BFEs of the MW–LMC system presented in S. Lilleengen et al. (2023) that are simulated using EXP (M. S. Petersen et al. 2022), with the expansion coefficients recorded at each time step.

The BFE technique uses appropriately chosen bi-orthogonal density-potential pairs of basis functions, $\{\varrho_\mu(x), \phi_\mu(x)\}$, that solve Poisson's equation, $\nabla^2\phi_\mu(x) = 4\pi G\varrho_\mu(x)$, and satisfy the bi-orthogonality condition, $\int d^3x\, \phi_\mu(x)\varrho_\nu(x) = 4\pi G\delta_{\mu\nu}$, where $\delta_{\mu\nu}$ is the Kronecker delta. Each basis function, labeled by the index μ, adds a degree of freedom to the system and has an associated coefficient A_μ, which determines its contribution to the total description of the system given by the summation over all basis function terms. A system at any given time is described by the basis functions and the coefficients that weight them. Mathematically, the density, ρ, and gravitational potential, Φ, are given by, $\rho(x, t) = \sum_\mu A_\mu(t)\varrho_\mu(x)$ and $\Phi(x, t) = \sum_\mu A_\mu(t)\phi_\mu(x)$, where the basis coefficients are time-dependent, and the basis functions keep their fixed functional form.

Basis functions are selected to reflect the system they describe. To model density profiles, $\rho(r, \phi, \theta)$, with deviations away from spherical symmetry, the spherical harmonics Y_l^m are chosen to describe the distribution in the angular coordinates (ϕ, θ), while EXP describes the radial dependence (index n) by the eigenfunctions of a Sturm-Liouville equation (M. D. Weinberg 1999). Each basis function is then represented by the triplet of indices $\mu \equiv (n, l, m)$. The radial index, n, determines the number of nodes in the radial basis function. It is often convenient to describe individual harmonic subsets of l. The $l = 0$ terms are called the monopole, $l = 1$ is the dipole, and $l = 2$ is the quadrupole. The EXP method creates a lowest-order monopole term, $\rho_{000}(r)$, that exactly matches the unperturbed, spherical, input potential-density pair. All other, higher-order, terms are perturbations around the input distribution. Another example of a BFE is the classical Hernquist–Ostriker basis set (L. Hernquist & J. P. Ostriker 1992), which expands upon the Hernquist density distribution (L. Hernquist 1990) as $\rho_{000}(r)$. This expansion has been used extensively in the literature (e.g., K. V. Johnston et al. 2001, 2002a, 2002b; J. L. Sanders et al. 2020). Alternative choices of analytic basis functions based upon the Navarro–Frenk–White profile (NFW; J. F. Navarro et al. 1997) have been made such that flattened density distributions are more accurately described (E. J. Lilley et al. 2018a, 2018b).

2.1.2. N-body Models

An efficient, lightweight Python interface, MWLMC, has been developed to facilitate the EXP simulations of the S. Lilleengen et al. (2023) MW–LMC system. This user-friendly interface is publicly available at: https://github.com/sophialilleengen/mwlmc. This MW–LMC system is made up of three constituents with separate BFEs: the MW dark matter halo,

the MW stellar disk and bulge, and the LMC dark matter halo. The EXP method explicitly uses the BFE for the force evaluations in the N-body evolution. We summarize all components in Table 1. Detailed descriptions of the BFE and N-body models can be found in S. Lilleengen et al. (2023).

The live simulation of the MW–LMC system begins at $t = -2.5$ Gyr, with the present day at $t = 0$ Gyr. The simulation aims to set the 6D present-day LMC coordinates with: an R.A. and decl. of (α, δ)=(78°.76 ± 0.52, −69°.19 ± 0.25), proper motions of (μ_α, μ_δ)=(1.91 ± 0.02, 0.229 ± 0.047) mas yr^{-1} (N. Kallivayalil et al. 2013), a distance of $d = 49.59 ± 0.54$ kpc (G. Pietrzyński et al. 2019), and a line-of-sight velocity of $v_{\rm los,} = 262.2 ± 3.4$ km s^{-1} (R. P. van der Marel et al. 2002). At the start of the live simulation, the MW and LMC haloes are totally distinct, with the LMC outside the virial radius of the MW at a distance of 450 kpc. The density, force, and potential fields before the start of the live simulation have the basis coefficients set to their initial values prescribed at $t_{\rm live}$.

2.2. Globular Cluster Populations in MW–LMC Systems

2.2.1. Initial Conditions—Present-day Gobular Cluster Distribution

To generate the present-day phase-space coordinates of our globular cluster sample, we draw samples from an ergodic distribution function implemented in AGAMA (E. Vasiliev 2019). This requires instances of a tracer density and potential profile. We use a Dehnen tracer density profile (W. Dehnen 1993) and an NFW profile for the potential (J. F. Navarro et al. 1997) that matches the rigid monopole order expansion of the MW halo potential used in S. Lilleengen et al. (2023; see also Section 2.1.2). We over-sample this distribution function to return a set of 3×10^5 possible present-day phase-space coordinates.

We impose certain criteria on the allowed range of orbits given the returned phase-space positions and velocities. We enforce the orbits to have a pericenter between 10 and 25 kpc, and an apocenter no greater than 75 kpc. The cut on the allowed orbital pericenter is to produce streams with sufficiently disrupted and extended tidal tails. Streams with pericenters smaller than this range begin to wrap and span the full longitudinal axis in progenitor coordinates; see Section 2.2.2. This makes our simple stream statistics in Section 3.2 difficult to interpret. Furthermore, allowing streams to orbit within heliocentric distances requires careful distinction between galactocentric and heliocentric quantities. The cut on the allowed progenitor apocenter, and pericenter, will limit the analysis to interesting streams that interact with the LMC near its pericenter and so do not spend large portions of time at very large Galactocentric radii. To determine the peri/apocenters for each final condition drawn from the distribution function, we integrate their orbits for 5 Gyr using GALA (A. M. Price-Whelan 2017). For the Galactic potential, we use the same prescription as used to instantiate the distribution function. These calculated peri/apocenters may differ from those calculated using a time-evolving potential. Of the orbits that pass these criteria, we take a random sample of 16,384 phase-space positions and velocities to be our present-day distribution of stream progenitors.

We model the density profile for each globular cluster as a Plummer sphere (H. C. Plummer 1911). This requires knowledge of the mass and scale radius of the cluster. To assign a mass to each cluster, $M_{\rm prog}$, we randomly draw values from the initial log-normal mass function shown in O. Y. Gnedin et al.

Table 1
Summary of the MW & LMC N-body Models

	MW Dark Matter Halo	MW Stellar Disk	MW Stellar Bulge	LMC Dark Matter Halo
Potential profile	Navarro–Frenk–White (J. F. Navarro et al. 1996, 1997)	Miyamoto–Nagai (M. Miyamoto & R. Nagai 1975)	Hernquist (L. Hernquist 1990)	Hernquist (L. Hernquist 1990)
Potential parameters	$M_{vir} = 7.92 \times 10^{11}\,M_\odot$	$M_{disc} = 6.8 \times 10^{10}\,M_\odot$	$M_{bulge} = 5.0 \times 10^{9}\,M_\odot$	$M_{LMC} = 1.25 \times 10^{11}\,M_\odot$
	$r_s = 12.8$ kpc	$a = 3.0$ kpc	$r_s = 0.5$ kpc	$r_s = 14.9$ kpc
	$c = 15.3$	$b = 0.28$ kpc		
N-body particles	10^7	10^6	10^6	10^7
l_{max}	6	…	…	6
m_{max}	…	6	6	…
n_{max}	17	17	17	23

Note. Virial quantities are defined by a sphere enclosing an overdensity that is 200 times the critical density of the Universe, $\rho_{crit} = 3H^2/8\pi G$, denoted with a "vir" subscript.

(2014, their Figure 2). The scale radius, a_s, is set to be 2 pc for every globular cluster (a suitable choice for globular clusters, e.g., the GD-1 globular cluster stream; A. M. Dillamore et al. 2022). We choose to consider only globular cluster streams, as, in the absence of external perturbations, they form dynamically cold and angularly (on-sky) thin stellar streams. These streams highlight stream perturbations due to the LMC and/or MW halo response more clearly than dynamically hotter dwarf galaxy streams.

2.2.2. Dynamical Modeling of Stellar Streams

We model stellar streams using a "modified Lagrange Cloud Stripping" (mLCS) technique (A. H. W. Küpper et al. 2012; A. Bonaca et al. 2014; S. L. J. Gibbons et al. 2014; A. Bowden et al. 2015; M. A. Fardal et al. 2015). Modifications were developed to include the forces from the LMC and the reflex motion of the MW in D. Erkal et al. (2019a). The stream progenitors are modeled as Plummer spheres (H. C. Plummer 1911) with initial masses and scale radii as defined in Section 2.2.1. Our mock stream implementation is similar to that in R. A. N. Brooks et al. (2024). We make sure to integrate orbits in the inertial frame of reference. By integrating orbits in noninertial frames of reference, this can result in fictitious, i.e., nonphysical, forces acting on streams (see, A. Arora et al. 2024b for discussion on inertial forces in cosmological simulations). This can lead to biases in stream fitting used to evaluate the Galactic potential. We discuss frames of reference and fictitious forces in Appendix A.

From the progenitor's present-day position, we rewind the phase-space orbit for 5 Gyr in a chosen MW–LMC potential; see Section 2.2.3. The system is subsequently forward-evolved in the same potential, and stream particles are released from the progenitor's Lagrange points, $r_{prog} \pm r_t$, at each time step. The Lagrange, or tidal, radius is found by, $r_t = (GM_{prog}(t)/(\omega^2 - d^2\Phi/dr^2))^{1/3}$, where ω is the angular velocity of the progenitor with respect to the MW, and $d^2\Phi/dr^2$ is the second derivative of the MW potential along the radial direction. Tidal stripping from the LMC is ignored. We model the mass loss of progenitors as linearly decreasing in time, such that they are fully disrupted at present day, since many progenitors are not seen in observational data at present day (S. E. Koposov et al. 2023). We account for the velocity dispersion of the progenitor, σ_v, by randomly drawing velocities from a 3D isotropic Gaussian centered on the velocities of the stripped particles, v_{strip}, with standard deviation $\sigma_v = \sqrt{GM_{prog}(t)/(r_t^2 + a_s^2)^{1/2}}$, where a_s is the scale radius of the progenitor. The radial component of v_{strip} is

the same as the progenitor, while the tangential components are set equal to those at the point halfway between the position of the progenitor and the Lagrange point.

To visualize the resulting stream, we rotate it into its own stream coordinates such that its progenitor lies at $(0°, 0°)$. To do this, we rotate around the z- and y-axes by the progenitor's longitude and latitude in Galactic coordinates, respectively. This defines a new x-axis about which we do a final rotation by the angular displacement of the progenitor's velocity vector. In Figure 1 we show this for three example streams generated in each potential we consider; see Section 2.2.3.

2.2.3. Galactic Potentials

We are interested in determining the effect on streams of direct LMC interactions and by the individual contributions to the full BFE description of the MW halo response. For the latter, we can selectively turn off harmonic terms of the full BFE, i.e., by setting all relevant BFE coefficients to zero, to isolate a given contribution to the total BFE description of the system. In this work, we consider nine unique potentials in which we generate a population of stellar streams. Figure 2 details the Galactic potentials used in this study. This table describes which individual potential components are included in the total potential; see Section 2.1.2. Additionally, we state whether each component is rigid or allowed to deform, and if so, which harmonic terms are included in the basis expansion. We also provide labels for each potential we use throughout this study and the associated color used in the Figures.

3. Results

3.1. Intuition and Expectations

The orbits of stellar streams in spherical potentials can be described entirely by their energy and angular momentum (K. V. Johnston 1998; A. Helmi 2020). For a Galactocentric frame of reference, the orbit of the stream will be contained to a single plane as angular momentum is conserved (C. Mateu 2023); this is the Great Circle orbit. Equivalently, in orbital pole space, as all stream stars will share similar and constant angular momentum, the spread in poles will be minimal. In the absence of perturbations, stream stars roughly delineate orbits that follow the stream progenitor (T. A. McGlynn 1990; K. V. Johnston et al. 1996; J. Binney 2008; J. L. Sanders & J. Binney 2013). This implies their velocities, or proper motions in projection, are aligned with the stream
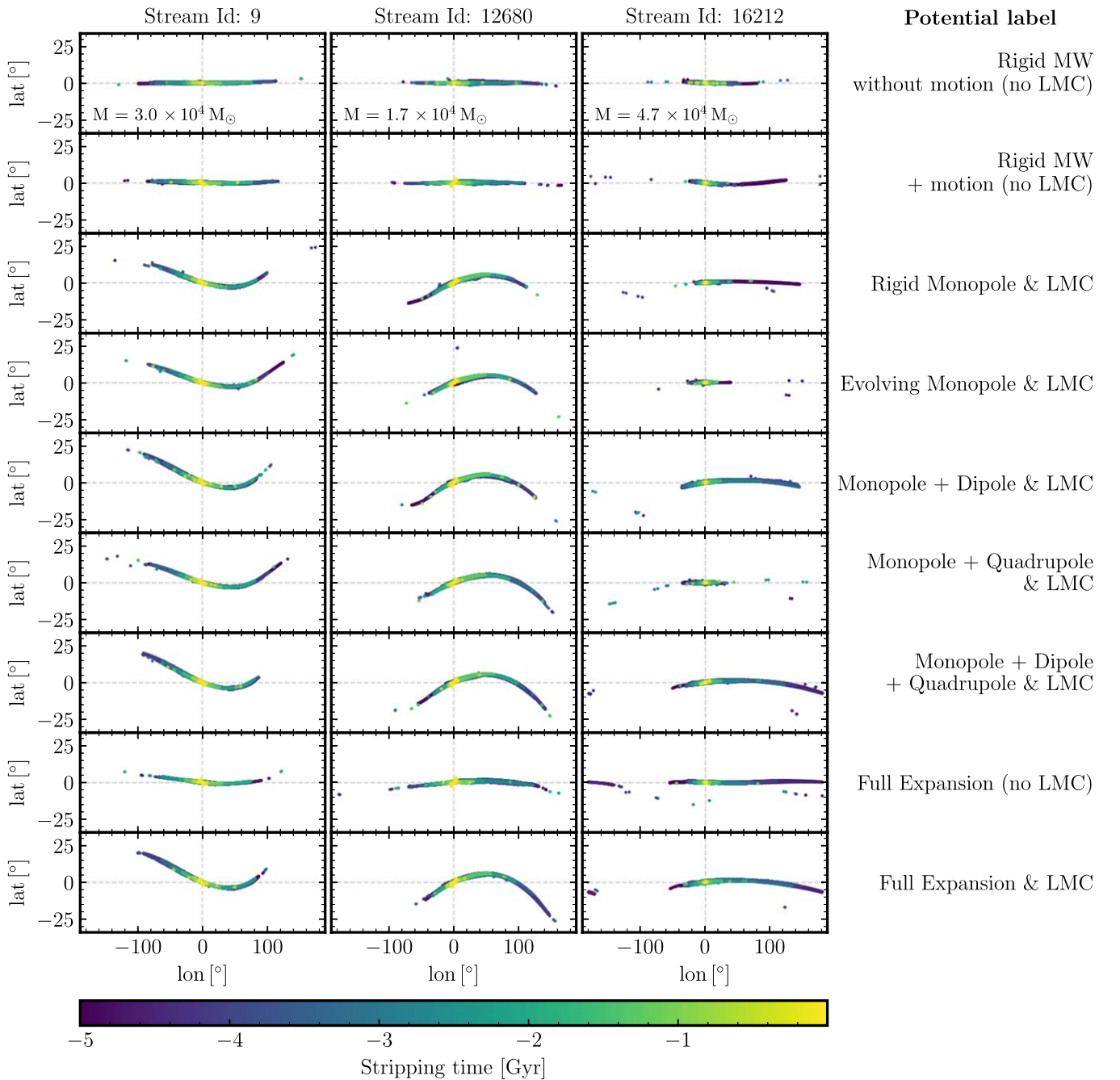
Figure 1. A selection of stellar streams generated using the present-day phase-space coordinates drawn from an ergodic distribution function and a progenitor mass assigned from a log-normal mass function; see Section 2.2.1. Each column shows an individual stream plotted in the coordinate frame centered on its progenitor; see Section 2.2.2. The "stream Id" is the column title, and the total stellar mass is shown in the top-row panels. The x-axis represents the longitude along the stream relative to the progenitor, such that positive/negative longitude corresponds to the leading/trailing tidal tail. The y-axis represents the latitude above the plane of the progenitor's orbit. Each row corresponds to the stream generated in an MW–LMC potential as labeled on the right-hand side; see Section 2.2.3. The color map shows the time at which the particles in the stream were tidally stripped from the progenitor relative to the present day, $t = 0$ Gyr. Each column illustrates the diversity in present-day stream morphology given the choice of Galactic potential.

track. Furthermore, the length of a stream is set by the time for which the progenitor has been tidally disrupting and its orbital frequency. The orbital frequencies vary along a stream such that the stars in the leading stream tail will have greater orbital frequencies than those in the trailing tail. Over time, this will cause a stream to be slightly asymmetric with bias toward longer leading tidal tails. The width of a stream is set by the scale over which debris is distributed; the tidal radius (K. V. Johnston 2016). Moreover, density variations along a stream reflect the number and frequency of visits to pericenter/

apocenter. At pericenter, tidal forces are maximal and the greatest amount of debris will be stripped from the progenitor. Conversely, the opposite is true at apocenter. This leads to periodic, or "epicyclic," over- and underdensities of stars along a stream equating to pericenter and apocenter passages (A. H. W. Küpper et al. 2008, 2010, 2012). By generating streams using a linear time step for orbit integration (see Section 2.2.2), we do not produce epicyclic density behavior. Nevertheless, this modeling choice does not alter any of our analysis.
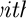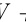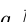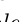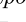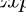
Potential label	Colour index	MW halo	$l_{\mathrm{exp,\,halo}}$	MW disc	$m_{\mathrm{exp,\,disc}}$	Reflex motion	LMC	$l_{\mathrm{exp,\,LMC}}$
Rigid MW without motion (no LMC)	▬	✓ (Rigid)	0	✓ (Rigid)	0	✗	✗	-
Rigid MW + motion (no LMC)	▬	✓ (Rigid)	0	✓ (Rigid)	0	✓	✗	-
Rigid Monopole & LMC	▬	✓ (Rigid)	0	✓ (Live)	0-6	✓	✓ (Live)	0-6
Evolving Monopole & LMC	▬	✓ (Live)	0	✓ (Live)	0-6	✓	✓ (Live)	0-6
Monopole + Dipole & LMC	▬	✓ (Live)	0, 1	✓ (Live)	0-6	✓	✓ (Live)	0-6
Monopole + Quadrupole & LMC	▬	✓ (Live)	0, 2	✓ (Live)	0-6	✓	✓ (Live)	0-6
Monopole + Dipole + Quadrupole & LMC	▬	✓ (Live)	0, 1, 2	✓ (Live)	0-6	✓	✓ (Live)	0-6
Full Expansion & LMC	▬	✓ (Live)	0 - 6	✓ (Live)	0-6	✓	✓ (Live)	0-6
Full Expansion (no LMC)	▪▪	✓ (Live)	0 - 6	✓ (Live)	0-6	✓	✗	-

Figure 2. Summary of the Galactic potentials used throughout this study, Section 2.2.3. The color index corresponds to the line colors used to represent each potential in the Figures.

When the Galactic potential becomes more complex (e.g., for time-independent axisymmetric, or triaxial, MW dark matter halo shapes), this leads to more complicated stream morphologies and evolution. In nonspherical potentials, a stream will broaden due to precession of the orbital planes of stream stars as the total angular momentum is no longer conserved (D. Erkal et al. 2016). Indeed, if the Hessian of the potential in action-angle coordinates has more than one eigenvalue with comparable magnitudes, a stream will form a multidimensional structure as opposed to the simple 1D structure (J. L. Sanders & J. Binney 2013). For example, streams close to the Galactic disk exhibit a range of vertical orbital frequencies forming 2D "ribbon"-like structures (W. Dehnen & Hasanuddin 2018). Additionally, for streams orbiting in regions of resonance, this further complicates the morphology of streams, e.g., "fans" of tidal debris for the Pal-5 stream (S. Pearson et al. 2015; A. M. Price-Whelan et al. 2016; T. D. Yavetz et al. 2021, 2023).

Interactions of streams with time-dependent structures in the Galaxy, such as the MW bar, can cause more rapid diffusion of streams (A. M. Price-Whelan et al. 2016), truncate the length of streams (K. Hattori et al. 2016), and lead to fanning of tidal debris (S. Pearson et al. 2017). The interactions of streams with dark matter subhaloes can cause "gaps" in streams to develop due to impulsive velocity kicks imparted on the stream (R. A. Ibata et al. 2002; K. V. Johnston et al. 2002b; J. H. Yoon et al. 2011; R. G. Carlberg 2012; D. Erkal & V. Belokurov 2015a; J. L. Sanders et al. 2016). Moreover, the interactions of streams with massive dwarf galaxies can affect their morphology, e.g., causing stream length asymmetries in the GD-1 stream (A. M. Dillamore et al. 2022). As the most recent dwarf galaxy merger, the LMC has caused disequilibrium in the MW (e.g., V. Belokurov et al. 2019; D. Erkal et al. 2019a, 2021; N. Garavito-Camargo et al. 2019; M. S. Petersen & J. Peñarrubia 2020, 2021; C. Conroy et al. 2021; E. Vasiliev et al. 2021; J. A. S. Amarante et al. 2024; V. Chandra et al. 2024; R. Yaaqib et al. 2024). The effect of the LMC on individual streams has been observed, e.g., Orphan-Chenab (D. Erkal et al. 2019b; S. E. Koposov et al. 2019; N. Shipp et al. 2019, 2021), but the general effect on the entire population of MW streams remains to be answered. In the following Sections, we address how the morphology and other stream observables are affected by their interactions with the LMC and/or via the MW halo response.

3.2. Summary Statistics

To quantify how the choice of Galactic potential affects the resulting stream population, we use a set of Galactocentric summary statistics motivated by the expectations above; see Section 3.1. We categorize these statistics into three parts: properties of the stream initial conditions, dynamical analysis, and direct observables. The initial condition statistics are defined by:

Progenitor mass. M_{prog} $[M_{\odot}]$, the mass of the progenitor before any tidal stripping occurs. This mass is also the total mass of the stellar stream at present day.

Pericenter. r_p [kpc], the radial distance from the center of the MW when the stream is at its closest position along its orbit. Calculated when integrating orbits in the time-independent potential; see Section 2.2.1.

Apocenter. r_a [kpc], the radial distance from the center of the MW when the stream is at its furthest position along its orbit. Calculated when integrating orbits in the time-independent potential; see Section 2.2.1.

For the dynamical analysis, we use the following statistics defined as:

Energy. E $[(\mathrm{km\ s^{-1}})^2]$, the Galactocentric energy of stream members. The energy for each stream particle is defined to be the sum of the kinetic plus potential energies.

Angular momenta. (L, L_z) $[\mathrm{km\ s^{-1}\ kpc}]$, the Galactocentric total and z-direction angular momenta of the stream particles.

Orbital poles. $(l'_{\mathrm{pole}}, b'_{\mathrm{pole}})$ $[°]$, using the stream particle positions and velocities in the Galactocentric Cartesian frame, we find the angular momentum vector as the cross product of the position and velocity vectors. We decompose the resulting vector into a normalized direction: the orbital pole, i.e., $\boldsymbol{J} = \boldsymbol{r} \times \boldsymbol{v} / |\boldsymbol{r} \times \boldsymbol{v}|$. We rotate the orbital poles with respect to the orbital pole direction of the MW disk, which we arbitrarily place at $(l', b') = (0°, 90°)$.

Additionally, for the stream observables, we use the following statistics, illustrated in Figure 3, defined as:

(Angular) length. l_{stream} $[°]$, the length of the stream in degrees. Taken between the 5th and 95th percentiles along the longitude in stream coordinates.

Asymmetry. $l_{\mathrm{leading}}/l_{\mathrm{trailing}}$, the ratio of the length of the stream leading and trailing tidal arms measured in degrees. For a perfectly symmetric stream, this ratio is equal to 1. A ratio
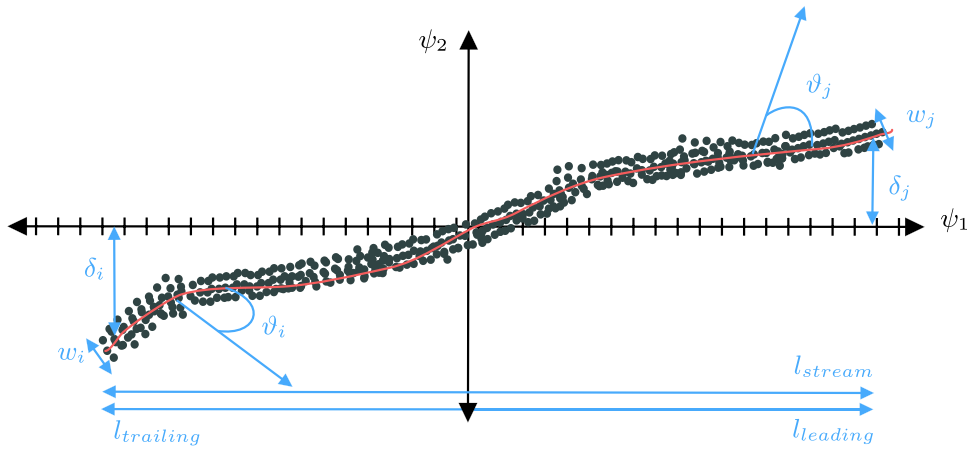
Figure 3. Illustration of how we measure the widths, w, lengths, l_{stream}, stream track deviation, δ, and proper-motion misalignment angle, ϑ as outlined in Section 3.2. Subscript notation indicates we measure each quantity in the ith to the jth bin in ψ_1. The axis represents the longitude ψ_1 and latitude ψ_2 of stream particles relative to the progenitor at $(0, 0)$. The Great Circle track is equivalent to $\psi_1 = 0°$. Example stream particles are shown as gray dots, with the red line through them representing the stream track.

above/below this value indicates a stream that is preferentially longer in its leading/trailing tidal arms.

- *(Angular) width. w [°]*, the width of the stream in degrees. We take 50 bins in the longitudinal stream coordinates, ψ_1. For each bin, we find the standard deviation of the corresponding latitudes, ψ_2, for stream particles. The width is then taken as the median value across all bins.

- *Deviation from Great Circle. $\bar{\delta}$ [°]*, the deviation of the stream in degrees from the unperturbed stream track, i.e., a Great Circle orbit. We take 50 bins in the longitudinal stream coordinates. For each bin, we find the absolute median latitude in stream coordinates; see Figure 3. As $\psi_2 = 0°$ corresponds to the Great Circle orbit, this angular value represents any deviation due to time-dependence in the potential. We quote the median value across all bins.

- *Local velocity dispersion: σ_v [km s^{-1}]*, the velocity dispersion of the stream across the width of the stream. We take 50 bins in the longitudinal stream coordinates between the 5th and 95th percentiles. For each bin, we find the standard deviation of stream particle velocities. The local velocity dispersion is taken as the median value across all bins.

- *Proper-motion misalignment: $\bar{\vartheta}$ [°]*, following C. Mateu (2023), we measure the angular separation between the angular momentum and the pole vector along the track. The misalignment angle is reported as the median value across the stream. The pole track is computed as the vector product between the adjacent position vectors along a stream. This pole track may change along the track if the stream is not perfectly planar. This is equivalent to D. Erkal et al. (2019b), who compared the tangent to the stream track with the ratio of proper motions along the track.

- *Orbital pole dispersion: $(\sigma_{l,\text{pole}}, \sigma_{b,\text{pole}})$ [°]*, the dispersion is calculated as the standard deviation of the orbital poles calculated for each stream particle as described in the preceding bullet.

3.2.1. Distributions of Summary Statistics

To analyze how the choice of Galactic potential affects the properties of a population of stellar streams, we plot the probability density functions in Figure 4 for the statistics that describe stream observables. In Figure 5 we plot the median, 16th–84th (black error bars) and 5th–95th (gray error bars) percentiles of these probability density functions. In Figure 4, we plot the fiducial "Full Expansion & LMC" potential as the thick solid black line and the "Full Expansion (no LMC)" as the thick dashed black line. By comparing these two potentials, we physically separate the direct influence of the LMC's gravity from the indirect effects of the MW halo response. The colored lines represent the distributions associated with potentials that use a subset, or rigid versions, of the full expansion MW BFEs; see Figure 2 for details. Relative comparison of these potentials will isolate effects resulting from harmonics of the MW halo response. For example, the comparison of the "Evolving Monopole & LMC" and "Monopole + Dipole & LMC" potentials isolates the importance of the MW dipole. Physically, the dipole is attributed to the displacement of the MW center of mass.

We find that some stream statistics are largely independent of the choice of Galactic potential used to generate the stream population. For example, the stream length, asymmetry, and velocity dispersion display similar distributions regardless of the potential. In Figure 5, this can be seen by the median and/or percentile boundaries being largely unaffected between potentials. The exception to this can be seen when the reflex motion of the MW barycenter is included. This effect lengthens some streams, increases the number of more significantly asymmetric streams, and increases the stream velocity dispersion.

We find that the stream statistics with clearer dependencies on the choice of Galactic potential used to generate a population of streams are: the widths, track deviations, proper-motion misalignments, and orbital pole spreads. In Figure 5, this is seen by the median and/or percentile boundaries changing between the potentials. By comparing the "Full Expansion & LMC" and the "Full Expansion (no LMC)" potentials, we can see the direct perturbation of the LMC as increasing the median value of these statistics. Moreover, the greatest change by response of the MW halo to the distributions is via its dipole harmonic. For these statistics, we want to find which are the best indicators for perturbations due to the LMC and the MW halo response, both
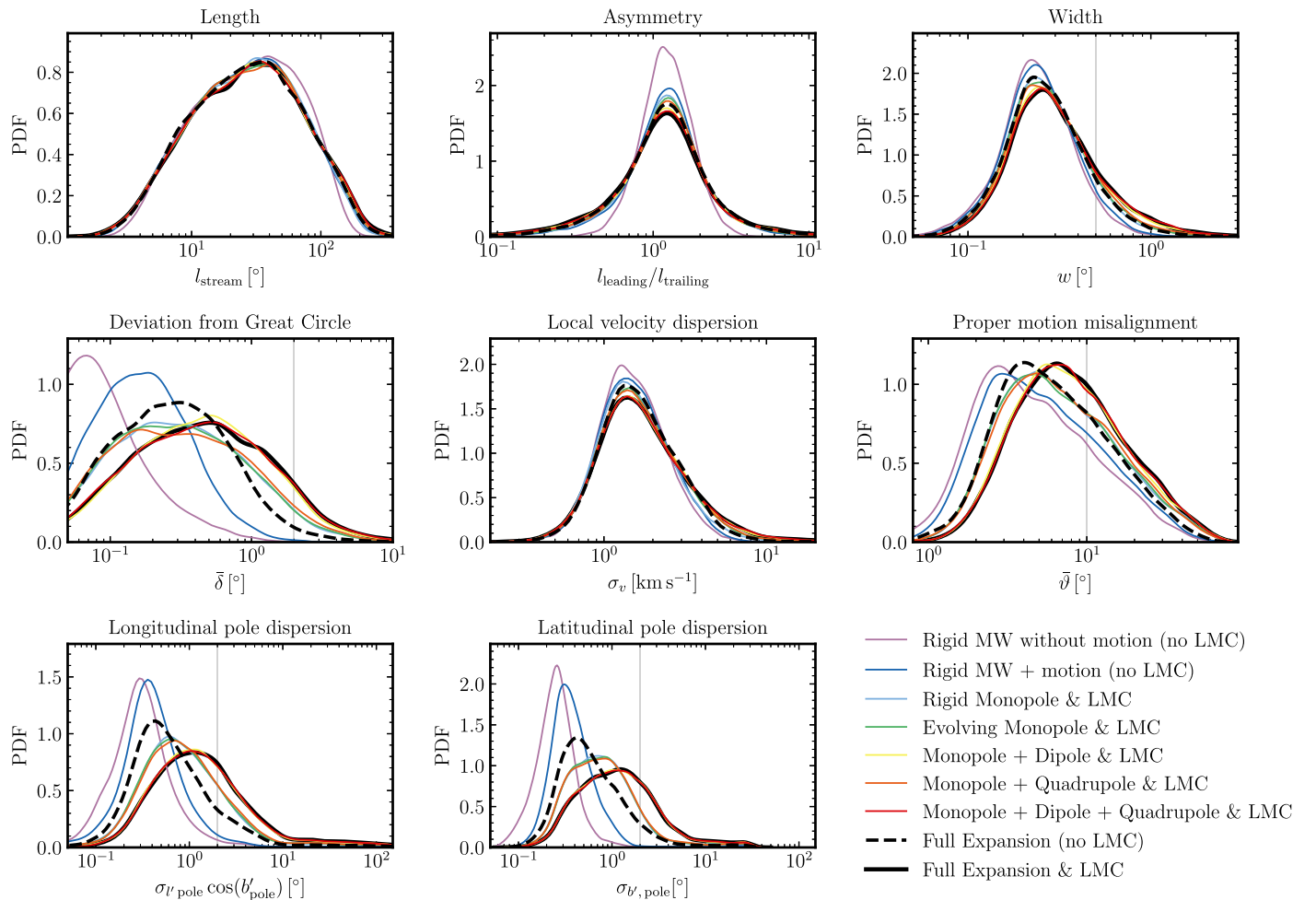
Figure 4. Probability density functions, inverse units of *x*-axes, for a selection of statistics that summarize stream observables. Left to right, and top to bottom, we show the length, l_{stream}, the asymmetry of the stream tidal tails, $l_{\text{leading}}/l_{\text{trailing}}$, the width, w, the track deviation from the progenitor's Great Circle orbit, $\bar{\delta}$, the local velocity dispersion, σ_v, the proper-motion misalignment angle $\bar{\vartheta}$, and the spreads in the longitudinal and latitudinal orbital poles rotated into the MW disk's orbital pole frame, $\sigma_{l',\text{pole}}$ and $\sigma_{b',\text{pole}}$. For each statistic, we plot lines associated with each potential in which we have generated a population of streams; see Figure 2 for details. The thick solid (dashed) black line shows the MW–LMC potential that is described by a full basis expansion MW with (without) a full basis expansion LMC. The statistics with the most striking differences between the potential used to generate the streams are the widths, track deviations, proper-motion misalignments, and orbital pole spreads. For these statistics, we draw a vertical gray line corresponding to the "detectable" threshold value we use to investigate LMC or MW halo response effects in Section 3.3.

as a function of Galactocentric distance and the on-sky angular position.

3.2.2. Detectable Stream Perturbations

For the stream statistics dependent on the Galactic potential: widths, track deviations, proper-motion misalignments, and orbital pole spreads, we propose "detectable" threshold values to capture the perturbations due to the LMC and the MW halo response. These threshold values are motivated by the expected observational values a stellar stream would display if there had been no external perturbations, i.e., stream properties are solely due to the intrinsic, physical processes that generate the stream itself. Hence, for streams that have summary statistic values greater than these threshold values, we associate these streams as being perturbed either directly by the LMC or by the response of the MW halo.

For a stream's width, this is controlled by the tidal radius, which depends on the Galactocentric distance and the masses of the progenitor and host galaxy (K. V. Johnston 1998). For a globular cluster, $\sim 10^4\,M_{\odot}$ in the MW, $\sim 10^{12}\,M_{\odot}$ over the

distances we consider, $\lesssim 75$ kpc, we can expect angular stream widths of $\sim 0°.5$. For the track deviations, we are motivated by the *galstreams* catalog of MW stellar streams (C. Mateu 2023). The great circle approximation is a good one when studying outer halo streams, $\gtrsim 25$ kpc, in a Galactocentric frame of reference. The *galstreams* catalog shows that more distant streams generally have smaller off-stream-plane deviations (see Figure 15 of C. Mateu 2023). Assuming the majority of the known most-distant streams are unperturbed, we adopt a threshold value of 2° to indicate perturbation due to an external source. For the proper-motion misalignments, we are motivated by the results of D. Erkal et al. (2019b) and C. Mateu (2023). The former highlights proper-motion perturbations to the Orphan-Chenab stream due to the LMC. Where the stream is most affected by the LMC, the proper-motion misalignment angle is always greater than $\sim 10°$. The orbital pole spreads depend on the spread of the positions, from the tidal radius, and velocities, from the velocity dispersion, of a stream. Using the values for these as motivated above, we can expect a pole spread of $\sim 1°$. For these statistics, we plot a vertical gray line in Figure 4 corresponding to their "detectable" threshold value.
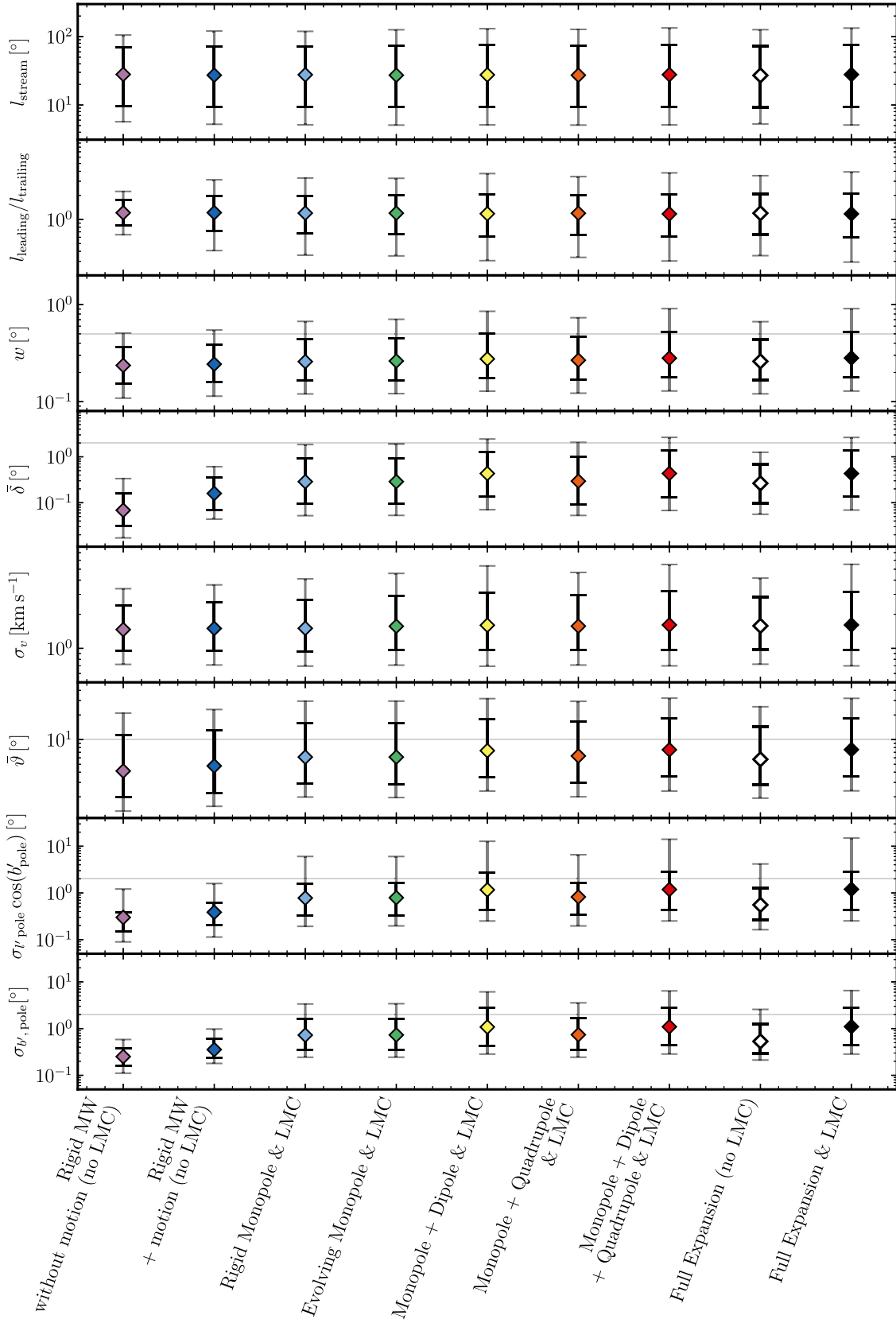
Figure 5. The median, 16th–84th (black error bars) and 5th–95th (gray error bars) percentiles of the stream statistic probability density functions in Figure 4 for each potential used to generate a population of streams; see Figure 2 for colors and description. Top to bottom we show the length, l_{stream}, the asymmetry of the stream tidal tails, $l_{\mathrm{leading}}/l_{\mathrm{trailing}}$, the width, w, the track deviation from the progenitor's Great Circle orbit, $\bar{\delta}$, the local velocity dispersion, σ_v, the proper-motion misalignment angle $\bar{\vartheta}$, and the spreads in the longitudinal and latitudinal orbital poles rotated into the MW disk's orbital pole frame, $\sigma_{l',\mathrm{pole}}$ and $\sigma_{b',\mathrm{pole}}$. We plot horizontal gray lines corresponding to the "detectable" threshold value we use to investigate LMC or MW halo response effects in Section 3.3.

Although these threshold values are physically and/or observationally motivated, there is still some subjectivity in their choice. The choice of threshold value will impact the amplitude of the fractional number of streams that display "detectable" perturbations. The most insightful results will come from the relative comparisons between potentials (see Section 3.3.1) and as a function of angular position on-sky (see Section 3.3.2). For small changes in the choice of threshold value, the qualitative result of this study remains unchanged. Furthermore, the Galactic potentials used in this work do not capture all sources of possible perturbation in the MW (see Section 3.1). Although it is beyond the scope of this work, it will be interesting to determine the extent to which other sources of perturbations (e.g., resonances with the MW bar; A. M. Dillamore et al. 2023, 2024) affect streams.

3.3. Trends of Stream Observables with Location

Section 3.2.1 demonstrated clear distinctions between the stream statistics distributions depending on the choice of Galactic potential used to generate the stream population. We want to know whether these distinctions occur in a particular, predictable locations of the Galaxy and whether the LMC and MW halo response effects are discernible. To achieve this, we adopt the detectable threshold values, as motivated in Section 3.2.2, to find the fraction of streams that have been significantly perturbed due to the LMC or the MW halo response. In Section 3.3.1, we then investigate how the fraction of perturbed streams varies radially outward through the MW halo. Furthermore, in Section 3.3.2, we investigate the angular dependence of any perturbations to determine whether a local signature of the LMC could be observed.

3.3.1. Radial Dependence

In Figure 6 we show the fraction of streams with detectable signatures of the LMC or MW halo response effect as a function of the stream progenitor's energy (lower x-axis), or equivalently, the progenitor's radial Galactocentric position (upper x-axis). We interpolate between energy and Galactocentric radius using the circular velocity profile of the MW halo. We plot the fiducial "Full Expansion & LMC" potential as the thick solid black line and the "Full Expansion (no LMC)" as the thick dashed black line. The colored lines represent the distributions associated with potentials that use a subset, or rigid versions, of the full expansion MW and LMC BFEs; see Figure 2 for details. The shaded regions around each line represent the Poisson uncertainty.

By comparing the "Full Expansion & LMC" and "Full Expansion (no LMC)" potentials, we are able to discern the direct gravitational influence of the LMC on streams. Strikingly, we find for the statistics considered that there is no overlap of these potentials within 1 standard deviation across large parts of the MW. The inclusion of the LMC in the potential significantly increases the fraction of streams with detectable perturbative features by ∼15%–25% for the proper-motion misalignments (∼25–70 kpc), and orbital pole spreads (∼20–50 kpc) stream statistics. On the other hand, only a ∼5% increase is seen in the deviation from a Great Circle orbit (∼15–45 kpc) and the widths of streams (∼25–70 kpc). These results imply that for the radial ranges stated, when we average stream statistics across the whole sky, we should be able to directly infer the gravitational impact of the LMC on MW streams given sufficient observational data.

The MW halo response captures how the dark matter halo reacts to the infalling LMC. By isolating individual contributions to the total response of the MW halo, e.g., the dipole harmonic, we are able to investigate how the inclusion of a harmonic mode in the global response affects the perturbations to MW streams. To determine this, we can compare the "Rigid Monopole & LMC" (light-blue line) potential to others that include an LMC but allow for time-variation and/or higher-order harmonics to be included in the MW halo BFE. Interestingly, there is no additional contribution to the fraction of streams affected when the monopole harmonic (green line), and/or the quadrupole harmonic (orange line), are allowed to be time-dependent and included in the MW halo expansion. Hence, the response of the MW is completely dominated by the inclusion of the dipole harmonic (yellow line; the MW halo dipole captures the reflex and center-of-mass motions). This increases the fraction of streams affected by up to, e.g., ∼30% for the latitudinal orbital pole spreads. This suggests that the monopole and quadrupole contributions to the MW halo potential are significantly weaker than the dipole, consistent with the findings of S. Lilleengen et al. (2023) and R. A. N. Brooks et al. (2024). Furthermore, any differences due to the MW halo harmonics appear to be systematic over the full Galactocentric distance shown.

The distributions of the various stream statistics in Figure 6 show contrasting radial profiles. For streams residing in the outskirts of the MW ≳30 kpc, the LMC has the greatest impact on their proper motions. Indeed, there is a positive correlation between the fraction of streams with detectable proper-motion changes and Galactocentric radius. At these distances for the fiducial MW–LMC potential, the fraction of streams with detectable misalignments of their proper-motion vectors relative to their stream track increases beyond 50%. Future surveys like LSST (Ž. Ivezić et al. 2019) at the Rubin Observatory are set to detect many more outer halo streams. As the amount of data increases, it will be interesting to see whether these predictions match the observations; see Section 4.2. For streams in the inner parts of the MW, ≲30 kpc, the track deviations, pole spreads, and widths of streams have their largest fraction of perturbed streams. These statistics all show negative correlations with Galactocentric radius. However, the inner halo streams do not always show discernible differences for the choice of Galactic potential. Nevertheless, inner halo streams appear to be more affected by the response of the MW halo than by the LMC itself, e.g., longitudinal pole spread.

3.3.2. Angular Dependence

To determine whether the LMC leaves a localized detectable signature, we investigate the properties of our stream population in the fiducial "Full Expansion & LMC" potential by dividing the Galactic all-sky view into quadrants. We visualize these quadrants in the lower-right panel of Figure 7 with the past orbit of the LMC colored by its Galactocentric distance. We define Quadrant 1 (Q1, orange) as $l \in \{+180°, 0°\}$, $b \in \{0°, +90°\}$, Quadrant 2 (Q2, green) as $l \in \{0°, -180°\}$, $b \in \{0°, +90°\}$, Quadrant 3 (Q3, purple) as $l \in \{+180°, 0°\}$, $b \in \{-90°, 0°\}$, and Quadrant 4 (Q4, pink) as $l \in \{0°, -180°\}$, $b \in \{-90°, 0°\}$.

In Figure 7 we show the same stream statistics as in Figure 6 except now only for the fiducial "Full Expansion & LMC" potential and split into these angular quadrants. For all of these statistics, Q4 (shown in bold) has the highest fraction of
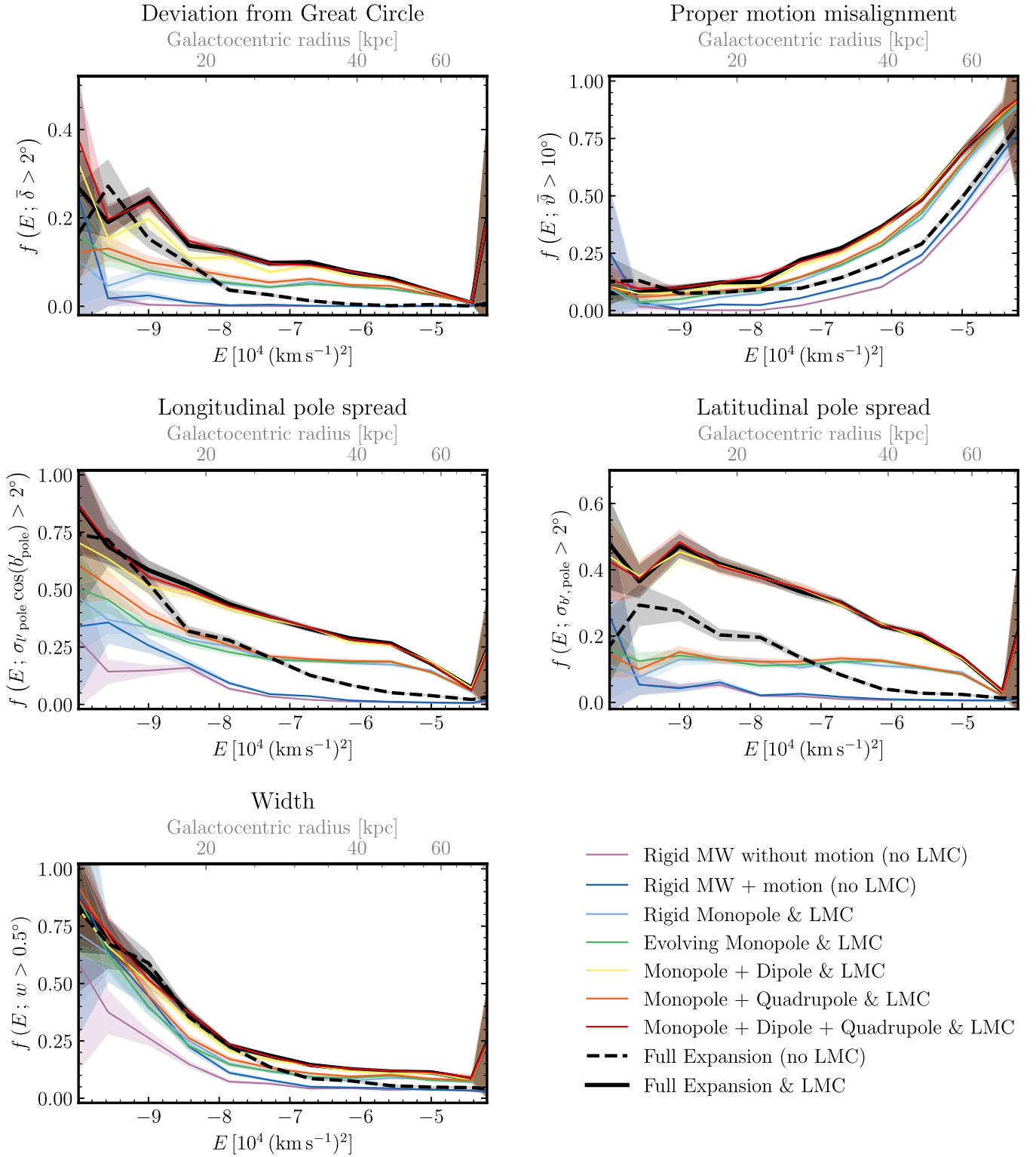
Figure 6. Fraction of streams with "*detectable*" signatures of the LMC as a function of the stream progenitor's energy (lower *x*-axis), or equivalently, radial Galactocentric position (upper *x*-axis). For each panel, a "detectable" signature in a stream at present day constitutes one in which: the deviation from the Great Circle track exceeds $2°$ (top left); the proper-motion misalignment exceeds $10°$ (top right); the spread in the longitudinal pole rotated into the MW disk's orbital pole frame exceeds $1°$ (middle left); the spread in the latitudinal pole rotated into the MW disk's orbital pole frame does not exceed $1°$ (middle right); and the stream width exceeds $0°.5$ (lower left). We plot lines associated with each potential in which we generate a population of streams; see Figure 2. The thick solid (dashed) black line shows the MW–LMC potential that is described by a full basis expansion MW with (without) a full basis expansion LMC. Poisson error bars are shown for each potential as the shaded region of the same color. In the inner/outer halo, the MW halo response / LMC dominates the effect on streams.

streams with detectable signatures of the LMC. At present day, the LMC resides in Q4 at a Galactocentric distance of ∼50 kpc having just completed its pericentric passage. Around this

distance, the detectable fraction of affected proper-motion misalignments and pole spreads are significantly higher, ∼30%, in Q4 compared to Q1, which is least affected.
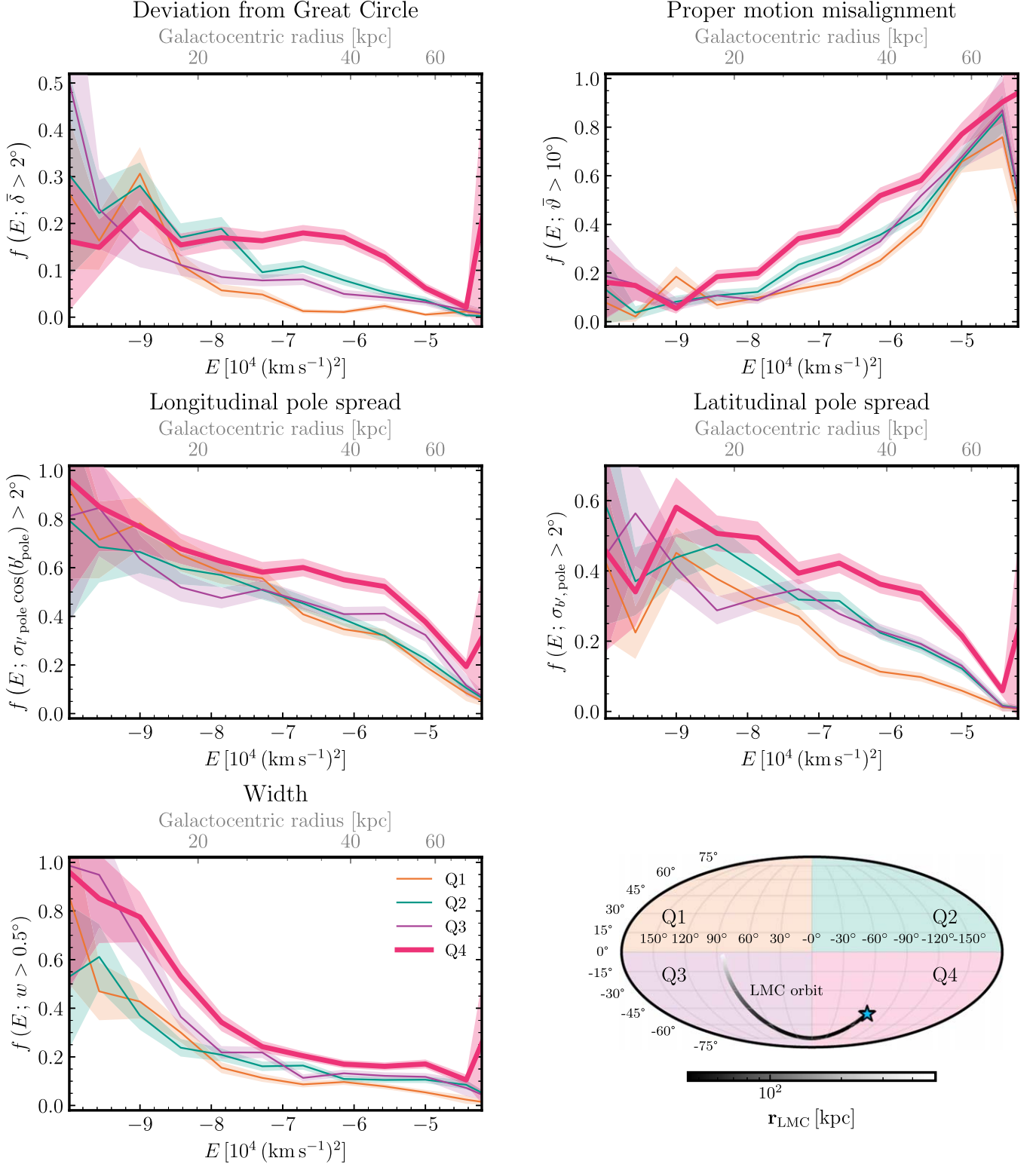
11

Figure 7. Same quantities as in Figure 6, now decomposed into quadrants in Galactic coordinates for the fiducial "Full Expansion & LMC" potential. The color scheme for each quadrant is reflected in the lower-right panel, which shows an all-sky projection in Galactic coordinates. The path of the LMC over the last 5 Gyr is over-plotted, and colored by its Galactocentric distance, with the present day depicted by the blue star. Within the uncertainties, the direct effect of the LMC in Q4 (bold line) is distinguishable between the on-sky quadrants. This suggests that observations of streams across the whole sky will show a localized LMC effect on these quantities.

Similarly, the track deviations and widths show this relative enhancement, albeit with a smaller amplitude, ∼10%–20% differences between Q4 and Q1. The relative enhancements between quadrants depend on properties of the adopted MW–LMC model. Hence, this provides a future opportunity to learn more about the MW–LMC system; see Section 5.2. This
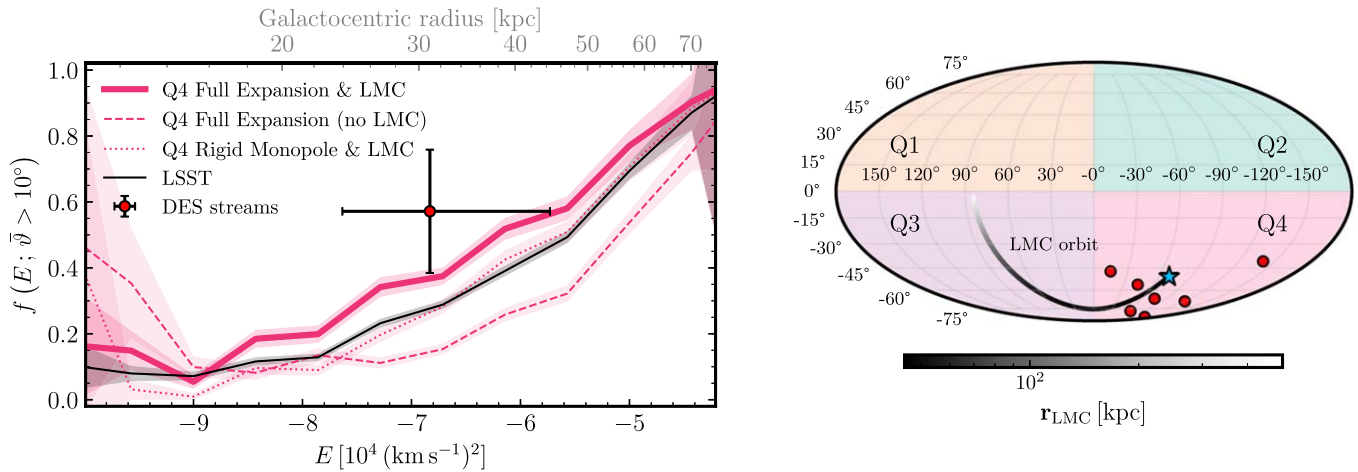
Figure 8. Left panel: the fraction of streams with a "*detectable*" signature of external perturbation in the misalignment of their proper motions with respect to the stream track as a function of the stream progenitor's energy (lower *x*-axis), or equivalently, radial Galactocentric position (upper *x*-axis). The thick solid pink line represents the "Full Expansion & LMC" potential in Q4 of the Galactic all-sky view; see the right panel. The dotted/dashed pink lines show the result for Q4 using an MW–LMC potential described by the "Rigid Monopole & LMC"/"Full Expansion (no LMC)" potential; see Figure 2. The black solid line represents the expected fraction for the footprint of the upcoming Rubin Observatory Legacy Survey of Space and Time (LSST; Ž. Ivezić et al. 2019). Poisson error bars are shown for each potential as the shaded region. The fraction of streams with detectable signatures as measured using the Dark Energy Survey (DES; N. Shipp et al. 2018, 2019) streams with proper-motion measurements is shown as the red circle with 1σ uncertainty. Right panel: all-sky projection in Galactic coordinates split into quadrants. The path of the LMC over the last 2.5 Gyr is over-plotted, and colored by its Galactocentric distance, with the present day depicted as the blue star. The positions of the DES streams are shown as red circles. All of these streams are in "Q4" where the LMC is at present day.

angular dependence clearly demonstrates there is a local effect of LMC of MW streams. There is a direct relationship between proximity to the LMC and the likelihood of a stream being significantly perturbed.

We replotted Figure 7 to show the results for the "Full Expansion (no LMC)" potential (not shown here). In this case, we find there is no angular dependence on the fraction of significantly perturbed streams for any of the stream statistics used, as might be expected for such a global perturbation via the MW halo response. These results motivate using streams as observational probes in all-sky surveys, as discussed in the next Sections.

4. Proper-motion Misalignments

To connect with observations, in Section 4.1 we take observational data from DES (N. Shipp et al. 2018, 2019) for streams that have proper-motion measurements and find the fraction of these observed streams that have detectable signatures in their proper motions, as defined in Section 3.2.2. We compare this against theoretical predictions for the misalignment angle given our simulated stream samples. We then make a prediction for the upcoming Rubin LSST (Ž. Ivezić et al. 2019) in Section 4.2.

4.1. Comparison to DES

We are able to compare our theoretical prediction for the fraction of streams with detectable signatures in their proper motions with stream data from DES. We are able to calculate the angular misalignment of the stream proper-motion vectors (N. Shipp et al. 2019) with respect to the stream track (N. Shipp et al. 2018). All of the DES streams reside in Q4, as shown in the right panel of Figure 8. The red points represent the Galactic coordinates of the DES streams. In the left panel of Figure 8, we show the result for the mean distance of the DES streams as the red point. The distance uncertainty is determined by the standard deviation of the DES stream distance data. The

fractional uncertainty is the binomial standard deviation. Additionally, we show the Q4 result for the "Full Expansion & LMC" (thick pink line), "Rigid Monopole & LMC" (pink dotted line), and "Full Expansion (no LMC)" (pink dashed line) potentials. Within uncertainty, the DES result agrees with our prediction for Q4 using the fiducial "Full Expansion & LMC" potential. However, this rudimentary measurement is subject to sample incompleteness. As the right panel of Figure 8 demonstrates, this measurement is mainly local to the immediate area surrounding the LMC; i.e., there is a large proportion of Q4 that has no currently observed streams. We tentatively expect the measured fraction of significantly affected streams to be lower and drop to be further in line with our prediction for Q4, as more of the quadrant is surveyed. Finally, the "Rigid Monopole & LMC" and "Full Expansion (no LMC)" potentials in Q4 predict much lower fractional values at the mean DES measurement distance, with $\sim 2\sigma$ significance. This further demonstrates the importance of the LMC in both causing the MW halo response and its direct gravitational influence, respectively.

4.2. Prediction for Rubin LSST

We are set to detect many more outer halo streams with the Rubin Observatory, in particular within the first 5 yr with LSST (Ž. Ivezić et al. 2019). Using the fiducial "Full Expansion & LMC" potential, we are able to forecast the expected fraction of streams with detectable signatures in their proper motions. To do this, we take the LSST sky footprint,[7] which covers the entire southern sky, and find the fraction of simulated streams that fall within its boundaries. We show the prediction for the LSST footprint in the left panel of Figure 8 as the solid black line. In comparison to the DES measurement, LSST will observe a lower fraction of significantly perturbed streams. This makes intuitive sense, as LSST covers an area of the sky

_____

[7] LSST GitHub repository (https://github.com/lsst/rubin_sim): Scheduler, survey strategy analysis, and other simulation tools for Rubin Observatory.

that is ∼3–4× larger; hence, regions of higher and lower fraction of perturbed streams will be averaged out. The power of LSST will be to probe the outermost halo streams, ≳40 kpc, and determine their properties. This will allow us to better constrain the properties of the LMC as the properties of streams beyond this radial distance will be sensitive to both the mass ratio and the infall trajectory of LMC; see Section 5.2.

5. Discussion

5.1. Reflex Motion of the MW

The reflex motion in our Galaxy refers to the motion about the common center of mass in the MW–LMC system. This displaces stars and other objects in the inner and outer parts of our Galaxy in unique ways (M. D. Weinberg 1995; F. A. Gómez et al. 2015; E. Vasiliev 2023). We have considered two potentials that highlight the relative importance of this effect on inner/outer halo streams, namely the "Rigid MW without motion (no LMC)" and "Rigid MW + motion (no LMC)." This reflex motion effect can be seen in Figure 6 for the longitudinal orbital pole spread and the width of streams. Within ≲25 kpc, the inclusion of the reflex motion drives statistically significant differences between the fraction of streams with detectable perturbations, and grows in magnitude toward the innermost part of the halo. Further, the probability density functions in Figure 4 demonstrate how the reflex motion affects the distribution of stream statistics. It causes nonnegligible effects on the orbital pole spreads and deviation from Great Circle orbits; however, these effects may not be "detectable," as the distributions do not have extended tails beyond the observational threshold values motivated in Section 3.2.1. It will remain the scope of future studies to seek the effect of the reflex motion on the population of inner halo MW streams.

5.2. Caveats

The nature of our methodology poses a handful of caveats. The first is our use of only a single MW–LMC idealized simulation (S. Lilleengen et al. 2023), which means we are unable to explore the dependence of our results on varying the masses of the MW, the LMC, or both simultaneously. There is a handful of idealized MW–LMC simulations that adopt different choices of the MW and LMC masses (e.g., N. Garavito-Camargo et al. 2019, 2021). Using these simulations would be the next step in understanding the effect of halo mass, and infall trajectory, on MW stream perturbations. The perfect scenario would be to have many MW–LMC simulations, with varying masses of both haloes, to explore this effect on stellar streams and allow for rapid inference in mass parameter space to find the "best-fit" masses. Cosmological simulations with analog MW–LMC pairs offer an alternative route to study this (e.g., the *Milky Way-est* simulations; D. Buch et al. 2024); although, the infall times and orbital properties of the LMC analog may not exactly match observational constraints. However, there remains considerable uncertainty in the orbital period and apocentric distance for the LMC (E. Vasiliev 2023). Furthermore, although idealized MW–LMC simulations allow for easier control of model parameters and intuition of how they affect results, they cannot capture the triaxiality of dark matter haloes that cosmological simulations are able to.

Another caveat comes from the choices of modeling the MW stream population. We choose an ergodic distribution function to draw the present-day positions and velocities of stream progenitors; see Section 2.2.1. Subsequently, this ensures that the generated stream distribution will be spatially isotropic. This approach will overlook any effects of clustering of streams, i.e., around the LMC. Plus, we do not model streams hosted by the LMC itself. Neglecting this population likely changes the predictions of angular on-sky dependencies for the fraction of significantly perturbed streams in Figure 7, as Q4 would have a higher number of streams relative to other quadrants. Further, we impose constraints on allowed orbital parameters. For a rigid MW potential, we would expect the proper motions of stream stars to be aligned with its track. However, in Figure 6, our rigid MW potential does not demonstrate this behavior at larger Galactocentric distances. This can be explained by the fact that the misalignment is calculated in a Galactocentric and not a reflex-corrected heliocentric reference frame. At these distances, streams will be at, or close to, their apocenter; hence, in the Galactocentric frame, their proper motions and stream track can be naturally misaligned. Therefore, the constraint on the allowed range of apocenters is degenerate with the expected fraction of streams with significantly misaligned proper motions.

Finally, we did not include a dark matter subhalo population, which may influence the dynamics and properties of the MW stream population. Modeling individual stream–subhalo interactions allows for the recovery of the mass and density profile of the subhalo (D. Erkal & V. Belokurov 2015b; A. Bonaca et al. 2019; T. Hilmi et al. 2024). Given the larger number of MW streams, a statistical approach would be to model a dark matter subhalo population and infer its cumulative effect on the population of streams (e.g., R. G. Carlberg & C. J. Grillmair 2013; A. Arora et al. 2024a; J. Nibauer et al. 2024; see the latter for a novel Hamiltonian perturbation theory approach to modeling stream–subhalo perturbations in flexible potentials). Predominantly, dark subhalo impacts have been summarized by the power spectrum of density variations they imprint in streams (N. Banik et al. 2021a, 2021b); although, this metric cannot always distinguish the cause of the density variation (e.g., R. Ibata et al. 2020). Furthermore, the summary statistics used in this work to investigate LMC-induced effects may also be affected by the cumulative effect of many stream–subhalo interactions. We endeavor to add a realistic MW subhalo population to the fiducial MW–LMC potential used in this study. This would allow us to self-consistently generate and evolve the MW stream population in the presence of a dark matter subhalo population.

5.3. Alternative Dark Matter Models

Often, MW–LMC simulations adopt collisionless cold dark matter to capture and study the deformations to the dark matter haloes of the MW and LMC (e.g., those used in this work; S. Lilleengen et al. 2023). In fact, the structure of the deformations depends on the chosen dark matter model. Using self-interacting dark matter instead would subject both haloes to additional forces that depend on the relative velocities of both haloes throughout the interaction (e.g., S. R. Furlanetto & A. Loeb 2002; M. Kaplinghat et al. 2016). Moreover, fuzzy dark matter (FDM) produces dynamically colder dark matter wakes with more granular structure (H. R. Foote et al. 2023). Plus, FDM naturally produces cored dark halo profiles, which

display different dynamical friction behavior compared to cusped profiles (J. I. Read et al. 2006). Furthermore, alternative gravity models (i.e., modified Newtonian dynamics) do not have dark matter haloes to deform. Therefore, there is no effect from dynamical friction due to the MW dark halo (e.g., L. Ciotti & J. Binney 2004; C. Nipoti et al. 2008). This would drastically alter the past orbit of the LMC (e.g., X. Wu et al. 2008; J. Schee et al. 2013), offering another route to constrain gravity and dark matter models.

6. Summary and Conclusions

In this work, we have explored the properties of stellar streams in time-dependent MW–LMC systems. For the first time, we have taken the approach to model a realistic stellar stream population in deforming MW–LMC systems. This has allowed us to statistically determine the significance of dynamical signatures imprinted into a set of stream summary statistics used to describe each stream. The statistics used are the stream length, asymmetry, width, deviation from Great Circle orbits, local velocity dispersion, proper-motion misalignment, and orbital pole dispersions. We investigated the radial and on-sky angular dependence of stream perturbations caused by the direct effect of stream-LMC interactions and/or the response of the MW dark matter halo. Our use of BFEs to describe the MW–LMC system allows us to flexibly alter the potential to investigate these effects. Our main conclusions are as follows:

1. For outer halo streams, the width, deviation from a Great Circle, proper-motion misalignment, and spread in orbital pole stream statistics are *dependent* on the choice of Galactic potential used to generate the MW stream population, particularly for those with and without an LMC; see Section 3.2.1 and Figure 4.
2. The direct effect of the LMC on streams is seen to increase the fraction of outer halo streams with "detectable" signatures of an external perturbation by up to, e.g., ∼25% in significantly misaligned proper motions compared to a potential without an LMC; see Section 3.3.1 and Figure 6. Furthermore, we find there is an on-sky angular dependence with the highest fractions for all statistics coinciding with the quadrant of the sky where the LMC is located at present day; see Section 3.3.2 and Figure 7.
3. The effect of the MW halo response is dominated by its dipole harmonic. This effect leaves a signature in the longitudinal and latitudinal pole spreads, distinct from the direct LMC influence, for streams at distances $\lesssim 25$ kpc. While the dipole and LMC effects are distinct, it is inconclusive whether this will be detectable. For an MW halo that is initially spherically symmetric, the monopole and quadrupole harmonics have little, if any, effect on further dynamically altering stream statistics; see Section 3.3.1 and Figure 6.
4. For outer halo streams, the length, asymmetry, and local velocity dispersion stream statistics show hardly any dependence on the choice of Galactic potential used to generate the MW stream population; see Section 3.2.1 and Figure 4.
5. We compare our prediction for the fraction of streams with significantly misaligned proper motions to the observational data from DES. Within uncertainty, our prediction agrees with the DES data despite an incomplete data sample; see Section 4.1 and Figure 8.
6. We make a prediction for the fraction of streams with significantly misaligned proper motions as a function of distance for the upcoming Rubin LSST survey. With more LSST data for outer halo streams, this will allow us to improve constraints on the properties of the LMC, e.g., its mass and infall trajectory; see Section 4.2 and Figure 8.

Our results have demonstrated that MW stellar streams are affected both directly by interactions with the LMC and by the response of the MW halo to the infalling satellite. The extent to which features of streams are affected is dependent on its radial and angular location. We find that we can, and already have, detected the direct influence of the LMC on streams within its immediate vicinity. All-sky surveys to find outer halo streams are increasingly important given the relative enhancement in the fraction of streams with "detectable" signatures across on-sky quadrants. The reflex motion, captured by the dipole of the MW halo response, appears to mostly affect streams in the inner MW halo. This motivates future studies committed to investigating the innermost streams in our Galaxy. With the advent of more stream data from Rubin LSST, we look forward to comparing our theoretical predictions with the data to better understand the MW–LMC interaction, properties of dark matter, and the LMC itself.

Data Availability

Greek mythology understands *Oceanus*,[8] Son of Gaia, to be the primordial Greek titan god of the great, earth-encircling stream $\Omega\kappa\epsilon\alpha\nu\sigma\varsigma$, and, among many other roles, the font of all fresh water, e.g., rain clouds. Hence we name our populations of simulated stellar streams generated after Oceanus. We publish the $t = 0$ Gyr simulation snapshots of all 16,384 streams in each MW–LMC potential used in this work. Each stream contains 20,000 particles with 3D Galactocentric positions and velocities, plus progenitor information on its initial conditions, mass, and scale radius. We do not include summary statistic values. The functions to calculate stream summary statistics will be shared upon reasonable request. This data set can be used to explore the effect of the LMC and the

---

[8] https://en.wikipedia.org/wiki/Oceanus

MW halo response on simulated MW streams. The archive with this data is hosted on Zenodo: doi:10.5281/zenodo.13771517 and doi:10.5281/zenodo.13771837. The python interface to integrate orbits and access to the expansion model for the S. Lilleengen et al. (2023) MW–LMC simulation can be found here:https://github.com/sophialilleengen/mwlmc.

Appendix A
Frames of Reference and Fictitious Forces

In this Appendix, we build upon Section 2.2.2 to describe the process we use to generate a stellar stream. The first step to generate a stream is to integrate the progenitor's orbit backward through the desired integration time. To achieve this, one must start from the present-day Galactocentric initial conditions drawn from the tracer Dehnen distribution function (W. Dehnen 1993). To ensure we integrate in the inertial frame of reference, we must account for the current displacement of the Galactic barycenter due to the merger with the LMC. To do this, we add the positions and velocities of the barycenter to the present-day Galactocentric phase-space coordinates, i.e., $r_{0,\text{inertial}} = r_{0,\text{galactocentric}} + r_{\text{barycenter}}$ and $v_{0,\text{inertial}} = v_{0,\text{galactocentric}} + v_{\text{barycenter}}$. We integrate the progenitor between successive time steps using the leapfrog integrator[9] implemented in GALA (A. M. Price-Whelan 2017). We adopt a constant time step of 2 Myr. We have checked this integrator against our own leapfrog implementation and recover the same orbital trajectory. The force evaluations at each time step are calculated using the MWLMC simulation of S. Lilleengen et al. (2023). We use the functions that return forces in the frame of reference of each individual component; e.g., the "*mwhalo_fields*" function returns the forces of the MW halo in its own reference frame. To shift each force evaluation to the inertial frame, we subtract the current expansion center for each component before evaluating the force using the "*expansion_centers*" function at each time, e.g., $a_{\text{halo,inertial}}(r - r_{\text{halo center}})$. When the progenitor has been integrated backward through the desired time, we subtract the barycenter displacement and motion at this time to return the initial conditions in the Galactocentric Cartesian frame, i.e., $r_{\text{f, galactocentric}} = r_f - r_{\text{barycenter}}$ and $v_{f,\text{galactocentric}} = v_f - v_{\text{barycenter}}$.

To generate the stellar stream, we begin from the cluster's initial conditions in the Galactocentric Cartesian frame. Again, to ensure forces are evaluated in the inertial frame, we first add the barycentric displacement and motion at the start time. The forward integration generates the stream via the mLCS technique (Section 2.2.2), with the forces evaluated in the inertial frame of reference. At the final saved output, we subtract the barycentric displacement and motion to return stream positions and velocities in the Galactocentric Cartesian frame.

The generation of a stellar stream must use the forces of the Galactic potential evaluated in the inertial frame of reference; otherwise, the stream will be subject to fictitious, nonphysical
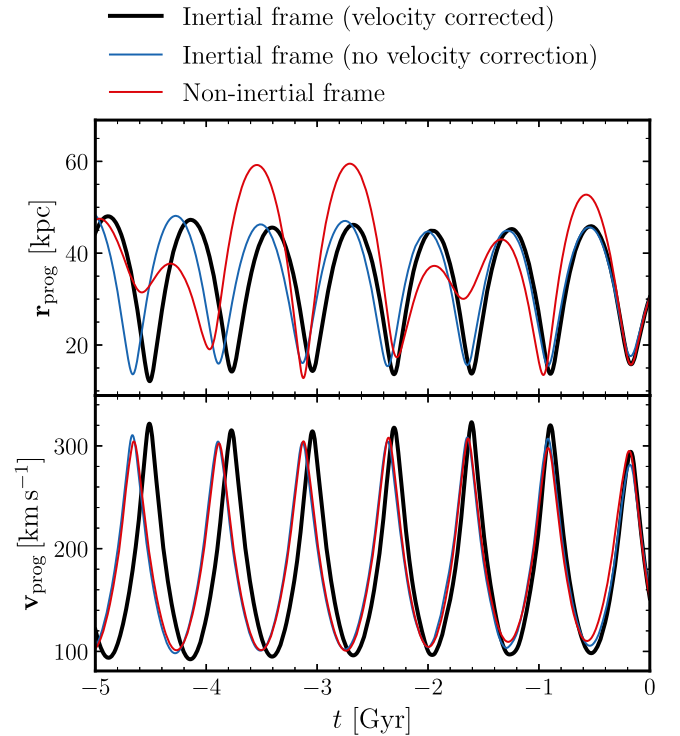

Figure 9. Example progenitor orbit when evaluating the forces for leapfrog integration in the frame of reference of the velocity-corrected inertial (thick black), the non-velocity-corrected inertial (blue), and the noninertial (red). The upper panel shows the radial positions, while the lower panel shows the magnitude of the velocity vector. A reproducible version of this Figure is available via this GitHub Gist (https://gist.github.com/dc-broo3/3ea3e8b15ebc2ad57d31f06cca5fbf75).

forces. Fictitious forces are pseudo-forces resulting from the frame of reference itself being accelerated or undergoing rotational motion. For example, if the forces are taken from the reference frame centered on the MW disk, this will include fictitious forces. If one integrates orbits using forces evaluated in a noninertial frame of reference, the resulting trajectory will be biased by these forces, which we would not see in observation. To illustrate this in Figure 9, we integrate an example progenitor ("*stream_0*" of our present-day globular cluster sample) in an MW–LMC potential described by the full BFEs; see Section 2.2.3. We use the integration forces by evaluating them in the velocity-corrected inertial (thick black), the non-velocity-corrected inertial (blue), and the noninertial (red) frames of reference. We show the progenitor's radial position and velocity magnitude throughout its orbit in the upper and lower panels of Figure 9, respectively. By not accounting for the motion of the MW barycenter, and/or evaluating forces in a noninertial frame of reference, the orbit of the progenitor varies drastically. The fictitious forces are apparent when comparing the noninertial frame to the velocity-correct inertial one, causing the past orbit to become chaotic.

---

[9] https://en.wikipedia.org/wiki/Leapfrog_integration

Appendix B
Distribution of Statistics within Streams

In the main body, we summarized the impact of perturbations on streams by using the median of statistics averaged over each stream. However, some streams may only be impacted along part of their length, so this choice may "wash out" some signal. To justify our choice of the median statistic across the entire stream, we make a comparison to the stream statistic value calculated in each bin across the streams; see Section 3.2. In Figure 10, we show the distributions of the statistics computed in each bin along the stream normalized by the median evaluated over all bins. For three randomly chosen streams from the populations in each potential, we show the distributions for the stream proper-motion misalignments, local velocity dispersions, and widths. In most potentials, the distributions are not significantly skewed, showing that all bins in each stream

are similarly affected. Furthermore, the normalized statistic distributions for each potential setup are similar, suggesting further statistics would not yield more discriminating power. This implies that, on average across our mock sample of streams, using other choices for the stream statistic would not qualitatively change the results. D. Erkal et al. (2019b) showed in their Figure 1 that the Orphan-Chenab stream is ∼200° long and reported proper-motion misalignments in ∼25° bins. In our Figure 5, we show that the median length of simulated streams in all potentials is ∼25°. Hence, on average, our streams are the same angular length as a single bin of the Orphan-Chenab stream, where definitive proper-motion misalignments are measured. Physically, this suggests that using median statistics to capture the behavior across an entire stream in our simulated samples is reasonable given recent observations. For streams that are significantly longer than ∼25°, this may not be fully representative.
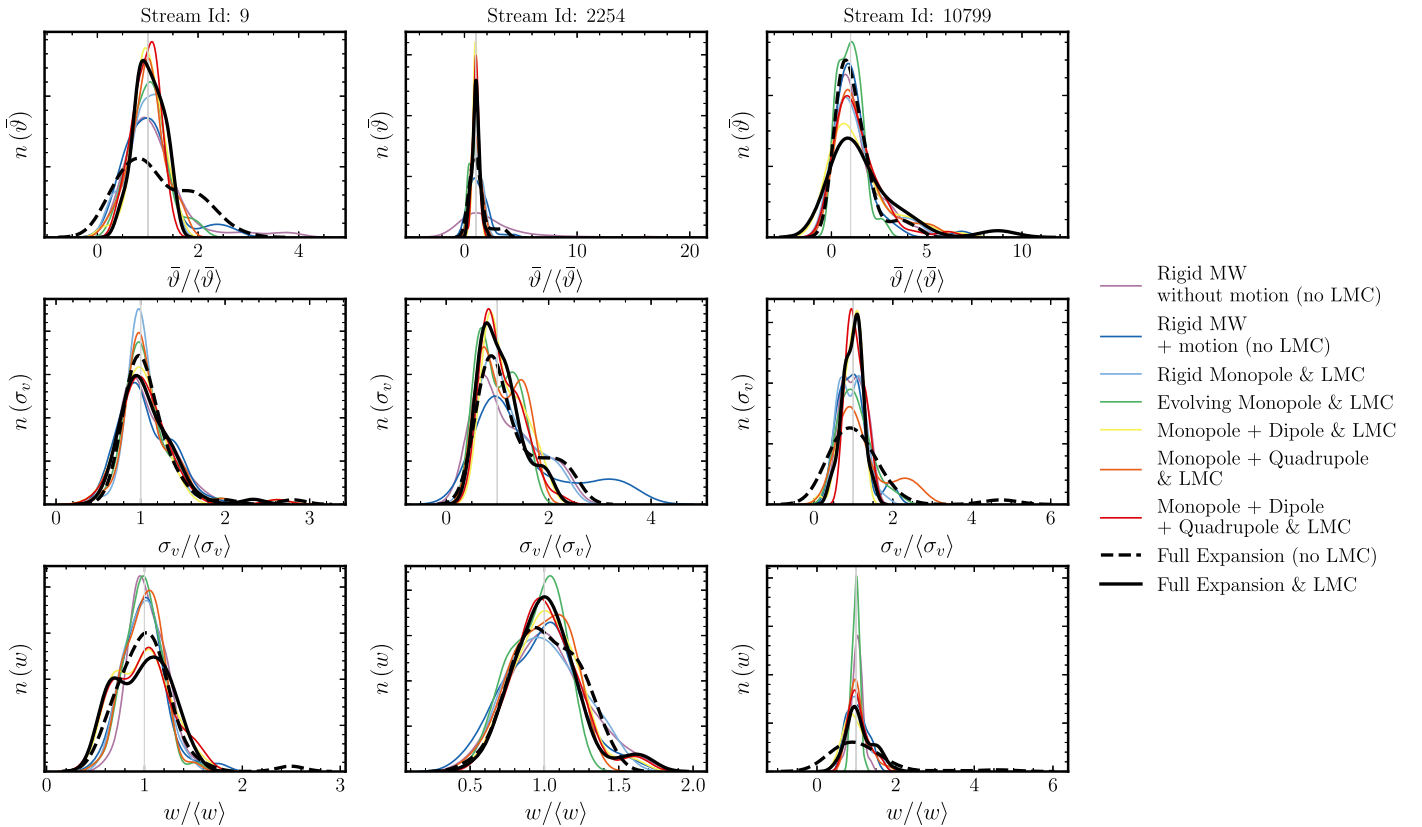

Figure 10. The distributions of the stream statistics computed in 50 equally spaced bins along three randomly selected streams for the different potential setups (see Figure 2). For each stream and potential, the distribution is normalized by the median stream statistic over all bins (as used throughout this study) and shown using a kernel density estimate. In rows top to bottom, we show the distributions for the stream proper-motion misalignments, local velocity dispersions, and widths. Each column represents a unique stream from the full simulated population, with the "stream Id" as the column title; see Section 2.2. In most potentials, the distributions are not significantly skewed. This implies that using other choices for the stream statistic would not qualitatively change the results in the main body.

ORCID iDs

Richard A. N. Brooks ⓘ https://orcid.org/0000-0001-5550-2057
Nicolás Garavito-Camargo ⓘ https://orcid.org/0000-0001-7107-1744
Kathryn V. Johnston ⓘ https://orcid.org/0000-0001-6244-6727
Adrian M. Price-Whelan ⓘ https://orcid.org/0000-0003-0872-7098
Jason L. Sanders ⓘ https://orcid.org/0000-0003-4593-6788
Sophia Lilleengen ⓘ https://orcid.org/0000-0001-9046-691X

References

Amarante, J. A. S., Koposov, S. E., & Laporte, C. F. P. 2024, A&A, 690, A166
Arora, A., Garavito-Camargo, N., Sanderson, R. E., et al. 2024a, ApJ, 974, 286
Arora, A., Sanderson, R., Regan, C., et al. 2024b, ApJ, 977, 23
Astropy Collaboration, Price-Whelan, A. M., Lim, P. L., et al. 2022, ApJ, 935, 167
Astropy Collaboration, Price-Whelan, A. M., Sipőcz, B. M., et al. 2018, AJ, 156, 123
Astropy Collaboration, Robitaille, T. P., Tollerud, E. J., et al. 2013, A&A, 558, A33
Banerjee, A., Adhikari, S., Dalal, N., More, S., & Kravtsov, A. 2020, JCAP, 2020, 024
Banik, N., Bovy, J., Bertone, G., Erkal, D., & de Boer, T. J. L. 2021a, MNRAS, 502, 2364
Banik, N., Bovy, J., Bertone, G., Erkal, D., & de Boer, T. J. L. 2021b, JCAP, 2021, 043
Belokurov, V., Deason, A. J., Erkal, D., et al. 2019, MNRAS, 488, L47
Benisty, D. 2024, A&A, 689, L1
Benisty, D., Vasiliev, E., Evans, N. W., et al. 2022, ApJL, 928, L5
Besla, G., Kallivayalil, N., Hernquist, L., et al. 2007, ApJ, 668, 949
Besla, G., Kallivayalil, N., Hernquist, L., et al. 2010, ApJL, 721, L97
Binney, J. 2008, MNRAS, 386, L47
Bonaca, A., Geha, M., Küpper, A. H. W., et al. 2014, ApJ, 795, 94
Bonaca, A., Hogg, D. W., Price-Whelan, A. M., & Conroy, C. 2019, ApJ, 880, 38
Bonaca, A., Pearson, S., Price-Whelan, A. M., et al. 2020, ApJ, 889, 70
Bonaca, A., & Price-Whelan, A. M. 2025, NewAR, 100, 101713
Bowden, A., Belokurov, V., & Evans, N. W. 2015, MNRAS, 449, 1391
Boylan-Kolchin, M., Besla, G., & Hernquist, L. 2011, MNRAS, 414, 1560
Brooks, R. A. N., Sanders, J. L., Lilleengen, S., Petersen, M. S., & Pontzen, A. 2024, MNRAS, 532, 2657
Buch, D., Nadler, E. O., Wechsler, R. H., & Mao, Y.-Y. 2024, ApJ, 971, 79
Carlberg, R. G. 2012, ApJ, 748, 20
Carlberg, R. G., & Grillmair, C. J. 2013, ApJ, 768, 171
Carlberg, R. G., Ibata, R., Martin, N. F., et al. 2024a, arXiv:2410.22966
Carlberg, R. G., Jenkins, A., Frenk, C. S., & Cooper, A. P. 2024b, ApJ, 975, 135
Cavieres, M., Chanamé, J., Navarrete, C., et al. 2024, arXiv:2410.00114
Chamberlain, K., Price-Whelan, A. M., Besla, G., et al. 2023, ApJ, 942, 18
Chandra, V., Naidu, R. P., Conroy, C., et al. 2024, arXiv:2406.01676
Chandrasekhar, S. 1943, ApJ, 97, 255
Ciotti, L., & Binney, J. 2004, MNRAS, 351, 285
Conroy, C., Naidu, R. P., Garavito-Camargo, N., et al. 2021, Natur, 592, 534
Correa Magnus, L., & Vasiliev, E. 2022, MNRAS, 511, 2610
Cunningham, E. C., Garavito-Camargo, N., Deason, A. J., et al. 2020, ApJ, 898, 4
Dai, B., Robertson, B. E., & Madau, P. 2018, ApJ, 858, 73
Dehnen, W. 1993, MNRAS, 265, 250
Dehnen, W., & Hasanuddin 2018, MNRAS, 479, 4720
Dillamore, A. M., Belokurov, V., & Evans, N. W. 2024, MNRAS, 532, 4389
Dillamore, A. M., Belokurov, V., Evans, N. W., & Davies, E. Y. 2023, MNRAS, 524, 3596
Dillamore, A. M., Belokurov, V., Evans, N. W., & Price-Whelan, A. M. 2022, MNRAS, 516, 1685
Donaldson, K., Petersen, M. S., & Peñarrubia, J. 2022, MNRAS, 513, 46
Erkal, D., & Belokurov, V. 2015a, MNRAS, 450, 1136
Erkal, D., & Belokurov, V. 2015b, MNRAS, 454, 3542
Erkal, D., Belokurov, V., Laporte, C. F. P., et al. 2019a, MNRAS, 487, 2685
Erkal, D., Belokurov, V., Laporte, C. F. P., et al. 2019b, MNRAS, 487, 2685
Erkal, D., Deason, A. J., Belokurov, V., et al. 2021, MNRAS, 506, 2677
Erkal, D., Koposov, S. E., & Belokurov, V. 2017, MNRAS, 470, 60
Erkal, D., Sanders, J. L., & Belokurov, V. 2016, MNRAS, 461, 1590
Fardal, M. A., Huang, S., & Weinberg, M. D. 2015, MNRAS, 452, 301
Foote, H. R., Besla, G., Mocz, P., et al. 2023, ApJ, 954, 163
Furlanetto, S. R., & Loeb, A. 2002, ApJ, 565, 854
Gaia Collaboration, Brown, A. G. A., Vallenari, A., et al. 2021, A&A, 649, A1
Garavito-Camargo, N., Besla, G., Laporte, C. F. P., et al. 2019, ApJ, 884, 51
Garavito-Camargo, N., Besla, G., Laporte, C. F. P., et al. 2021, ApJ, 919, 109
Gibbons, S. L. J., Belokurov, V., & Evans, N. W. 2014, MNRAS, 445, 3788
Gnedin, O. Y., Ostriker, J. P., & Tremaine, S. 2014, ApJ, 785, 71
Gómez, F. A., Besla, G., Carpintero, D. D., et al. 2015, ApJ, 802, 128
Harris, C. R., Millman, K. J., van der Walt, S. J., et al. 2020, Natur, 585, 357
Hattori, K., Erkal, D., & Sanders, J. L. 2016, MNRAS, 460, 497
Helmi, A. 2020, ARA&A, 58, 205
Helmi, A., & White, S. D. M. 1999, MNRAS, 307, 495
Hernquist, L. 1990, ApJ, 356, 359
Hernquist, L., & Ostriker, J. P. 1992, ApJ, 386, 375
Hilmi, T., Erkal, D., Koposov, S. E., et al. 2024, arXiv:2404.02953
Hui, L., Ostriker, J. P., Tremaine, S., & Witten, E. 2017, PhRvD, 95, 043541
Hunter, J. D. 2007, CSE, 9, 90
Ibata, R., Thomas, G., Famaey, B., et al. 2020, ApJ, 891, 161
Ibata, R. A., Lewis, G. F., Irwin, M. J., & Quinn, T. 2002, MNRAS, 332, 915
Ivezić, Ž., Kahn, S. M., Tyson, J. A., et al. 2019, ApJ, 873, 111
Johnston, K. V. 1998, ApJ, 495, 297
Johnston, K. V., Choi, P. I., & Guhathakurta, P. 2002a, AJ, 124, 127
Johnston, K. V., Hernquist, L., & Bolte, M. 1996, ApJ, 465, 278
Johnston, K. V., Sackett, P. D., & Bullock, J. S. 2001, ApJ, 557, 137
Johnston, K. V., Spergel, D. N., & Haydn, C. 2002b, ApJ, 570, 656
Johnston, K. V., Zhao, H., Spergel, D. N., & Hernquist, L. 1999, ApJL, 512, L109
Johnston, K. V. 2016, Astrophysics and Space Science Library, Vol. 420, Tidal Streams in the Local Group and Beyond (Berlin: Springer)
Kallivayalil, N., van der Marel, R. P., Besla, G., Anderson, J., & Alcock, C. 2013, ApJ, 764, 161
Kaplinghat, M., Tulin, S., & Yu, H.-B. 2016, PhRvL, 116, 041302
Kawata, D., Baba, J., Hunt, J. A. S., et al. 2021, MNRAS, 508, 728
Kim, S. Y., Peter, A. H. G., & Wittman, D. 2017, MNRAS, 469, 1414
Koposov, S. E., Belokurov, V., Li, T. S., et al. 2019, MNRAS, 485, 4726
Koposov, S. E., Erkal, D., Li, T. S., et al. 2023, MNRAS, 521, 4936
Kravtsov, A., & Winney, S. 2024, OJAp, 7, 50
Küpper, A. H. W., Kroupa, P., Baumgardt, H., & Heggie, D. C. 2010, MNRAS, 401, 105
Küpper, A. H. W., Lane, R. R., & Heggie, D. C. 2012, MNRAS, 420, 2700
Küpper, A. H. W., Macleod, A., & Heggie, D. C. 2008, MNRAS, 387, 1248
Lancaster, L., Giovanetti, C., Mocz, P., et al. 2020, JCAP, 2020, 001
Lilleengen, S., Petersen, M. S., Erkal, D., et al. 2023, MNRAS, 518, 774
Lilley, E. J., Sanders, J. L., & Evans, N. W. 2018a, MNRAS, 478, 1281
Lilley, E. J., Sanders, J. L., Evans, N. W., & Erkal, D. 2018b, MNRAS, 476, 2092
Mateu, C. 2023, MNRAS, 520, 5225
McGlynn, T. A. 1990, ApJ, 348, 515
Miyamoto, M., & Nagai, R. 1975, PASJ, 27, 533
Mulder, W. A. 1983, A&A, 117, 9
Navarro, J. F., Frenk, C. S., & White, S. D. M. 1996, ApJ, 462, 563
Navarro, J. F., Frenk, C. S., & White, S. D. M. 1997, ApJ, 490, 493
Nibauer, J., Bonaca, A., Spergel, D. N., et al. 2024, arXiv:2410.21174
Nipoti, C., Ciotti, L., Binney, J., & Londrillo, P. 2008, MNRAS, 386, 2194
Patel, E., Besla, G., & Sohn, S. T. 2017, MNRAS, 464, 3825
Patel, E., Kallivayalil, N., Garavito-Camargo, N., et al. 2020, ApJ, 893, 121
Pearson, S., Bonaca, A., Chen, Y., & Gnedin, O. Y. 2024, ApJ, 976, 54
Pearson, S., Küpper, A. H. W., Johnston, K. V., & Price-Whelan, A. M. 2015, ApJ, 799, 28
Pearson, S., Price-Whelan, A. M., & Johnston, K. V. 2017, NatAs, 1, 633
Peñarrubia, J., Gómez, F. A., Besla, G., Erkal, D., & Ma, Y.-Z. 2016, MNRAS, 456, L54
Petersen, M. S., & Peñarrubia, J. 2020, MNRAS, 494, L11
Petersen, M. S., & Peñarrubia, J. 2021, NatAs, 5, 251
Petersen, M. S., Weinberg, M. D., & Katz, N. 2016, MNRAS, 463, 1952
Petersen, M. S., Weinberg, M. D., & Katz, N. 2019, MNRAS, 490, 3616
Petersen, M. S., Weinberg, M. D., & Katz, N. 2022, MNRAS, 510, 6201

Pietrzyński, G., Graczyk, D., Gallenne, A., et al. 2019, Natur, 567, 200
Plummer, H. C. 1911, MNRAS, 71, 460
Price-Whelan, A. M. 2017, JOSS, 2, 388
Price-Whelan, A. M., Sesar, B., Johnston, K. V., & Rix, H.-W. 2016, ApJ, 824, 104
Read, J. I., Goerdt, T., Moore, B., et al. 2006, MNRAS, 373, 1451
Rose, J. C., Torrey, P., Villaescusa-Navarro, F., et al. 2024, arXiv:2405.00766
Sameie, O., Creasey, P., Yu, H.-B., et al. 2018, MNRAS, 479, 359
Sanders, J. L., & Binney, J. 2013, MNRAS, 433, 1813
Sanders, J. L., Bovy, J., & Erkal, D. 2016, MNRAS, 457, 3817
Sanders, J. L., Lilley, E. J., Vasiliev, E., Evans, N. W., & Erkal, D. 2020, MNRAS, 499, 4793
Schee, J., Stuchlík, Z., & Petrásek, M. 2013, JCAP, 2013, 026
Shipp, N., Drlica-Wagner, A., Balbinot, E., et al. 2018, ApJ, 862, 114
Shipp, N., Erkal, D., Drlica-Wagner, A., et al. 2021, ApJ, 923, 149
Shipp, N., Li, T. S., Pace, A. B., et al. 2019, ApJ, 885, 3
Shipp, N., Panithanpaisal, N., Necib, L., et al. 2023, ApJ, 949, 44
Tamfal, T., Mayer, L., Quinn, T. R., et al. 2021, ApJ, 916, 55
Tavangar, K., Ferguson, P., Shipp, N., et al. 2022, ApJ, 925, 118

van der Marel, R. P., Alves, D. R., Hardy, E., & Suntzeff, N. B. 2002, AJ, 124, 2639
Vasiliev, E. 2019, MNRAS, 482, 1525
Vasiliev, E. 2023, Galax, 11, 59
Vasiliev, E. 2024, MNRAS, 527, 437
Vasiliev, E., & Baumgardt, H. 2021, MNRAS, 505, 5978
Vasiliev, E., Belokurov, V., & Erkal, D. 2021, MNRAS, 501, 2279
Virtanen, P., Gommers, R., Oliphant, T. E., et al. 2020, NatMe, 17, 261
Weinberg, M. D. 1986, ApJ, 300, 93
Weinberg, M. D. 1995, ApJL, 455, L31
Weinberg, M. D. 1999, AJ, 117, 629
Wu, X., Famaey, B., Gentile, G., Perets, H., & Zhao, H. 2008, MNRAS, 386, 2199
Yaaqib, R., Petersen, M. S., & Peñarrubia, J. 2024, MNRAS, 531, 3524
Yavetz, T. D., Johnston, K. V., Pearson, S., Price-Whelan, A. M., & Hamilton, C. 2023, ApJ, 954, 215
Yavetz, T. D., Johnston, K. V., Pearson, S., Price-Whelan, A. M., & Weinberg, M. D. 2021, MNRAS, 501, 1791
Yoon, J. H., Johnston, K. V., & Hogg, D. W. 2011, ApJ, 731, 58